ARTICLE

fib WILEY

Estimation of the bar stress based on crack width measurements in reinforced concrete structures

Enrique Corres | Aurelio Muttoni

School of Architecture, Civil and Environmental Engineering, Ecole Polytechnique Fédérale de Lausanne, Lausanne, Switzerland

Correspondence
Enrique Corres, School of Architecture, Civil and Environmental Engineering, Ecole Polytechnique Fédérale de Lausanne, Lausanne, Switzerland.
Email: enrique.corressojo@epfl.ch

Abstract

Estimating the stress of reinforcing bars and its variations in service conditions can be useful to determine the reserve capacity of structures or to assess the risk of fatigue in the reinforcement. This paper investigates the use crack width measurements to estimate the stress in the bars. In existing structures, crack width formulations can be used to estimate the stress in the reinforcement from crack width measurements, profiting from additional information that can be measured in-situ, such as the crack spacing. Recent experimental results show that the values of the mean bond stress typically considered in code formulations overestimate the actual bond stresses activated in cracked concrete specimens. This paper presents the results of an experimental program consisting of reinforced concrete ties and beams instrumented with Digital Image Correlation and fiber optical measurements. The results confirm the differences with typically assumed bond stresses. A formulation to estimate the bond stresses in service conditions is derived from the results of the numerical integration of a previously developed local bond–slip relationship. Their pertinence for the estimation of the stress in the reinforcement from the measured crack width is evaluated with satisfactory results for monotonic loading and for the maximum force in cyclic tests.

KEYWORDS
beam, bond stress, bond–slip, crack width, cracking, reinforced concrete, reinforcement stress, tie

1 | INTRODUCTION

Understanding the cracked response of reinforced concrete structures is important, as it influences the stiffness of members (deflections and vibrations) and their water tightness. Furthermore, crack control is important for durability and aesthetic reasons. Accordingly, current design standards such as Eurocode 2 (EC2:2004)[1] or *fib* Model Code 2010 (MC2010)[2] include expressions to estimate the crack width and impose limits based on the environmental exposure and other criteria.

Unsurprisingly, cracks are often found in existing structures and they are one of the indicators used in visual inspections for structural assessment.[3,4] However, the evaluation of the structural safety based on the presence or absence of cracks is not straightforward. On the one hand, cracks do not necessarily indicate an insufficient level of safety, if they are expected and coherent with the structural behavior of the structure. On the other hand, small crack openings might not be an indicator of sufficient resistance in cases governed by fragile failure modes.[4,5]

Considering the long service life of European structures[6–8] and the increase of traffic over the past decades[9] and its expected growth in the future,[10] the needs for monitoring existing structures are likely to increase in coming years. In this context, the availability of state-of-the-art tools to evaluate the state of existing structures is crucial to plan effective intervention strategies in large infrastructure networks. Additional information about the stress state of the bars can be useful to determine the dangerousness of a detected crack or the reserve capacity of existing structures.

The stress in the reinforcement and its variations are determining factors for the fatigue verification. The fatigue assessment of reinforcing bars in existing structures can be conducted in an efficient manner by measuring indirectly the stress variations. This can be conducted by measuring the strain variations in the bar using strain gauges, like in steel structures.[11] However, the disturbance of bond due to the removal of the concrete cover to glue the strain gauges can affect the results. An interesting alternative is provided by measuring the crack opening variations (using conventional or modern techniques such as Digital Image Correlation) and calculating the stress variations on the basis of bar stress – crack width relationships. However, crack formulations have the opposite goal: to estimate the crack width from the calculated reinforcement stress.[1,2] This results in simplifying assumptions that might not be pertinent if the formula is used in reverse for bar stress estimation. Moreover, in the case of existing structures, additional information such as crack spacing, which is an essential parameter in the crack width formulations, or the existence of secondary or splitting cracks can be measured or visually verified.

The first proposed crack width formulae were based on the slip, which is defined as the relative displacement between the steel and the concrete. When the crack appears, compatibility of deformations between the steel and the concrete is lost. The slip activates bond stresses which determine the crack spacing and the tensile stress distributions in the bar and the concrete.

Starting in 1936, Saliger[12] proposed a formulation based on this principle to calculate the crack spacing and width in flexural elements with smooth bars assuming a linear bond stress distribution with a maximum at the crack location. Thomas[13] proposed analytical expressions including the effect of shrinkage and assuming a parabolic bond stress distribution. A different approach was adopted by Brooms,[14] who assumed that no slip occurs between the bar and the concrete and that plane sections do not remain plane. In these conditions, tensile stresses develop linearly from the cracks leading to the generation of principal or secondary cracks, depending on whether they reach the surface of the concrete. The resulting crack spacing is proportional to the cover.[15] Ferry-Borges[16] proposed a formulation accounting for both effects that is the base of some of the current code formulae.[1,2] Several crack formulations can be found in the literature using different approaches (thorough reviews of the available models can be found in[17–19]). The comparison of 30 formulations performed by Lapi et al.[18] shows that the semi-analytical models of EC2:2004[1] and MC2010[2] are among the most accurate models. It must be noted that cracking is a highly variable phenomenon and even the best models have coefficients of variation close to 30%, compared with experimental results.[18]

Concerning the bond stresses, Balazs[20] proposed an analytical model based on the integration of the ascending branch of the bond–slip relationship for well-confined conditions from the *fib* Model Code 1990.[21] A closed form solution was proposed for the crack propagation stage, and a numerical integration was used for the stabilized cracking phase. Based on the analytical integration of a bond–slip relationship,[22] Sigrist[23] proposed a rigid plastic bond–slip law with a bond stress equal to $2f_{ctm}$ before yielding and f_{ctm} after bar yielding. The considered bond–slip laws[21,22] were derived from a relatively small number of tests. Recent research has shown that the bond–slip relationship from MC2010 captures the general trends of the interface response, but the influence of some parameters is not satisfactorily accounted for.[24–26]

Some attempts have been made to estimate the bar stress from surface crack measurements. Campana et al.[27] used the model by Sigrist[23] to estimate the stresses in the stirrups of beam tests based on crack width measurements; however, the results could not be verified, as the stirrups were not instrumented. Calvi[28] proposed a model for the assessment of elements with shear cracks, where the bar strains are estimated from crack width measurements using the expressions for proposed by Shima et al.[29] and the considerations of Maekawa et al.[30] Brault et al.[31] used this model to predict the strains measured in small beams subjected to bending instrumented with Digital Image Correlation (DIC) and distributed fiber optical sensors glued to the reinforcing bars. The estimated strains have the same order of magnitude as the measurements; however, the trends of the experimental results and the predictions show significant differences. Carmo et al.[32] estimated the average steel strain based on the results of ties with internally strain gauged bars and marker photogrammetry. They concluded that this approach is feasible, but the accuracy was limited by the camera resolution.

Recent experimental studies using DIC and distributed fiber optical sensors in ties[24,33–35] and beams[5,33,36,37] have shown great potential to improve the understanding

of the cracking process and the bar-to-concrete interaction. Some of these results show average bond stress values significantly lower than the code formulations.[34,36] Fiber optic sensors have proven to be useful to characterize shrinkage induced strains in the reinforcement.[34,35,38,39]

Based on these observations and the fact that bond plays a critical role in the cracking response, this paper investigates the development of bond stresses through analytical and experimental work, with the aim of improving the existing crack formulations to estimate the reinforcement stress based on crack width measurements. Given its mechanical basis, the slip approach is considered in this publication. First, the slip-based model is presented and the influence of the different parameters is evaluated. Secondly, experimental results from tie and beam tests instrumented with DIC and fiber optical sensors on the reinforcement are analyzed to better understand the cracking phenomenon and bond development. Lastly, new values for the bond stresses are proposed on the basis of a local bond stress–slip model adapted from Corres et al.[40] The slip-based model with the proposed bond values are used to estimate the stresses in the experimental results, showing satisfactory results.

2 | CRACKING IN STRUCTURAL MEMBERS

2.1 | Slip-based model

The mechanical behavior of a cracked element in tension is typically characterized by the force-average strain response, as shown in Figure 1a. The response can be divided in three phases. First, the uncracked response is

characterized by compatibility of strains between the bar and the concrete. The crack formation stage begins with the first crack, that appears when the tensile strength of the weakest concrete section is reached, leading to the strain distribution shown in Figure 1c. Bond stresses progressively transfer the force from the bar to the surrounding concrete that eventually reach the cracking strain again, at a distance that cannot be shorter than l_{cr} from the 1st crack. When all crack distances are not larger than $2l_{cr}$, new cracks cannot develop (end of the crack formation phase). The minimum and maximum crack spacings (s_{cr}) are thus l_{cr} and $2l_{cr}$, respectively. At this point, the stabilized cracking phase starts, characterized by an increase of the steel strains when the force is further augmented, see Figure 1c. This publication focuses on the stabilized cracking stage as it is the most relevant for structural members subjected to external loads.

The slip δ_{sc} corresponds to the difference between the displacements of the steel and the concrete. The slip in the differential element shown in Figure 1b can be calculated from the steel (ε_s) and concrete strains (ε_c) using Equation (1). The crack width results from the slip at each side of the crack (i.e. the crack spacing s_{cr}) as per Equation (2).

$$d\delta_{sc} = (\varepsilon_s - \varepsilon_c)dx, \tag{1}$$

$$w = \int_{s_{cr}} (\varepsilon_s - \varepsilon_c)dx = s_{cr}(\varepsilon_{sm} - \varepsilon_{cm}). \tag{2}$$

The stress and strain distributions in the two materials are determined by the external loads and the bond forces. A common approach in numerous crack models is
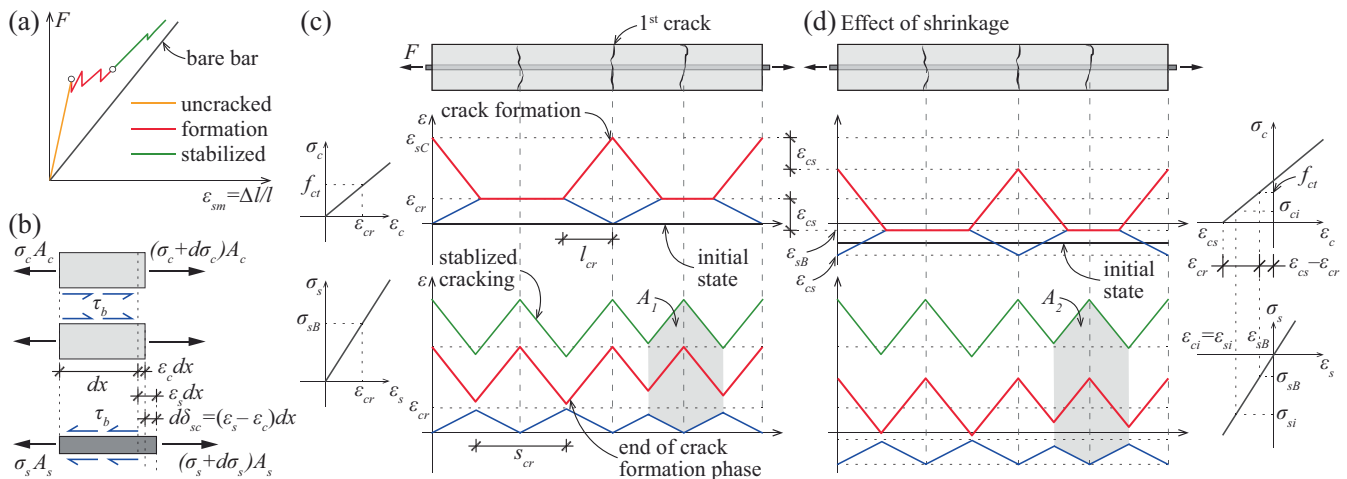

FIGURE 1 Response of a concrete tie: (a) force–average strain diagram; (b) differential tie element; strain distribution in the crack formation phase and the stabilized cracking phase (c) without the effect of shrinkage and (d) accounting for shrinkage.

to use a constant bond stress corresponding to the average over the bonded length ($\tau_{b,avg}$). This leads to the diagrams presented in Figure 1c where the strain profiles vary linearly. The residual tensile strength of the concrete[41] is neglected.

Shrinkage influences the initial stress and strain distributions (Figure 1d) and can reduce the cracking force.[42,43] According to Equation (2), the crack width corresponds to the area between the strain profiles of the bar and the concrete (areas A_1 and A_2 in Figure 1c,d). The effect of shrinkage can clearly be observed: for a given stress in the bar, the crack width is larger compared with the case neglecting shrinkage ($A_1 < A_2$). This is reflected in Equation (3) that allows to calculate the resulting crack width for a given bar stress in the stabilized cracking phase.

$$w = \frac{s_{cr}}{E_s}\left[\sigma_{sC} - \frac{s_{cr}\tau_{b,avg}}{\varnothing}\frac{1+(n-1)\rho_t}{1-\rho_t} - E_s\varepsilon_{cs}\right], \quad (3)$$

where E_s is the elastic modulus of the reinforcement, σ_{sC} is the stress in the reinforcement at the crack location, $\varnothing$ is the bar diameter, $n = E_s/E_c$, ρ_t is the reinforcement ratio of the tie and ε_{cs} is the unrestrained shrinkage strain (considered as a negative value, see Figure 1d). The derivation of this expression can be found in Appendix A.

This expression is the basis of the design crack width formulations in the current codes. MC2010 specifies the average bond strength in the calculation of the length over which slip between concrete and steel occurs. The proposed values for the average bond strength are $1.8f_{ctm}$ for short term loading and $1.35f_{ctm}$ for other types of loading. EC2:2004 does not explicitly mention the average bond stress. A factor to account for the casting position[44,45] has been included in the *fib* Model Code 2020 (MC2020)[46] and the second generation of Eurocode 2 (EC2:2023),[47] which leads to average bond stresses of $2f_{ctm}$ and $1.5f_{ctm}$ in good and poor casting conditions, respectively. The proposed expressions for the relative mean strain are similar with a factor to account for short or long-term loading.

The Tension Chord Model (TCM)[48] uses the same approach assuming a rigid plastic bond–slip relationship with bond stresses of $2f_{ctm}$ and $1f_{ctm}$ before and after yielding of the reinforcement.

A sensitivity analysis for a tie with a section of 100×100 mm and a reinforcement bar of Ø18 is presented in Figure 2. Figure 2a shows the bar stress–crack width diagram according to EC2:2004 (dashed black line), MC2010 (solid gray line) and Equation (3) (solid black line) for the reference value of the influencing parameters. For a given stress, the code formulations underestimate the crack width compared with Equation (3), because the stress variation is calculated assuming the maximum crack spacing. Figure 2b shows the influence of the different parameters. It can be observed that the crack spacing is a crucial parameter, which is favorable for existing structures as it can be measured
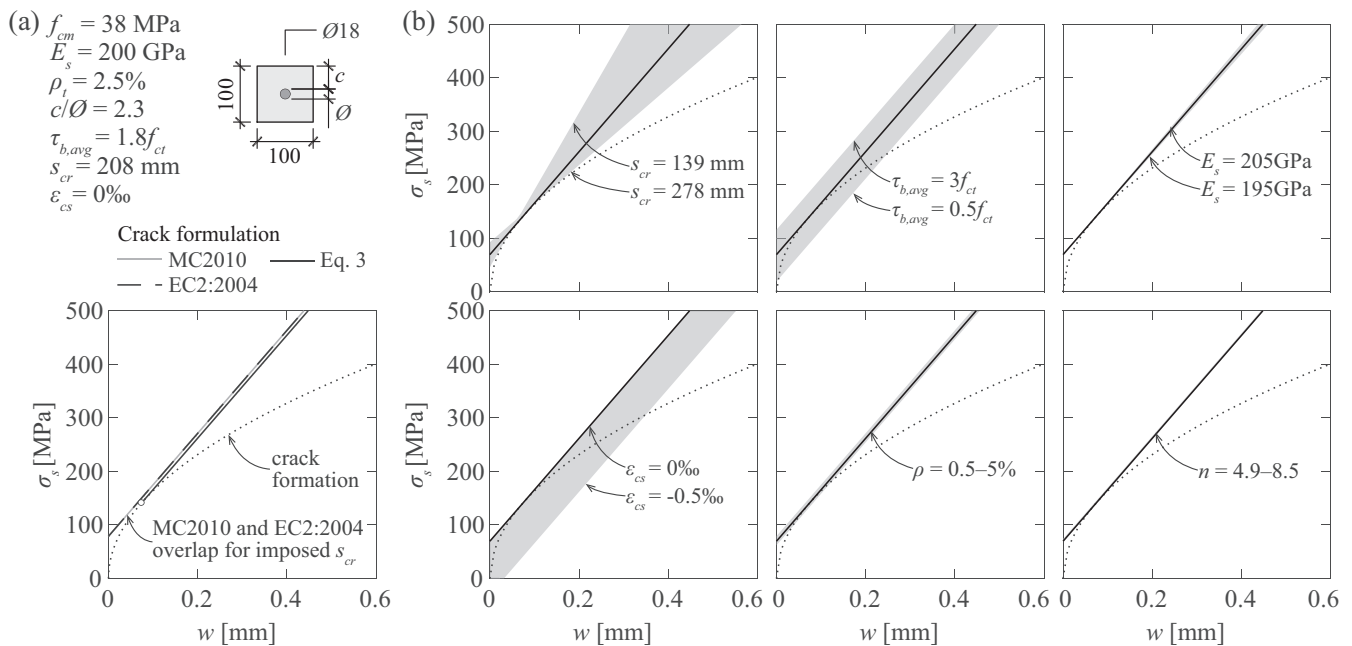

FIGURE 2 Sensitivity analysis of the influencing parameters in the bar stress–crack width relationship: (a) reference parameters and model comparison; and (b) effect of crack spacing, average bond stress, elastic modulus of steel, unrestrained shrinkage strain, reinforcement ratio and elastic moduli ratio.

with a certain precision. The effect of shrinkage is non-negligible. Estimating the shrinkage effects is difficult in simple specimens in laboratory conditions,[49] and even more so in real structures. However, as shrinkage strains induce compressive stresses in the reinforcement, by neglecting this effect a conservative estimate of the stress is obtained. Bond stresses have a relevant contribution particularly for small crack widths. The influence of the other parameters is relatively small.

2.2 | Elements subjected to bending

The cracking response of beams subjected to bending presents some differences with respect to the response of ties.[45] The stress distribution in the concrete near the bar is not uniform, cracks appear when the tensile strength of concrete is reached in the most tensioned face. The curvature of the section leads to different crack widths at the level of the reinforcement and at the most tensioned face. The variation of width implies that there is region of the section near the tip of the crack where crack widths are small ad where the residual tensile strength of concrete might influence the behavior. Due to the internal forces, beams often present more complex crack patterns with considerable variations in terms of crack width.[14,50–53] Furthermore, small and large beams typically display different crack patterns.[51]

The slip-based model is also used for elements subjected to bending by assuming an equivalent tie. Different definitions of the effective concrete area in tension can be found in the literature.[1,2,36,46,54] EC2:2004 accounts for the difference in the concrete stress distribution through a factor in the crack spacing formula. MC2010 does not consider this difference. Recently, Pérez Caldentey et al.[45] addressed this topic and proposed a factor to better consider the stress distribution near the reinforcement that has been included in *fib* Model Code 2020[46] and the second generation of Eurocode 2.[47]

2.3 | Additional experimental evidence

The reality is more complex than the response of the idealized concrete members described in the previous subsections. Experimental evidence shows that both the crack patterns and the distribution of bond stresses can differ from the description of the model.

Different types of cracks can be found in concrete ties. The first type is traversing cracks that cross the entire section of the tie and appear when the tensile strength of the concrete is reached in the full section. These are also referred to as primary cracks[55–57] or main cracks[34,58] by different authors. The second type is originated by the internal conical cracks that appear at the tip of the rib lugs due to the activation of bond stresses.[59] These internal cracks were first reported by Goto[55] and can become visible on the concrete surface, particularly for small covers. These cracks can eventually propagate to become traversing cracks. Some authors refer to these cracks as secondary cracks.[34,55,57] However, the term secondary crack is also used by some authors to refer to cracks that develop without reaching the surface of the specimen.[14] A third type are splitting cracks, these longitudinal cracks develop along the reinforcement near the traversing cracks[34,55] due to the splitting forces generated by bond.[25,59] In this paper, the cracks in the ties are categorized as traversing, non-traversing or splitting cracks.

Publications analyzing cracking of beams subjected to bending often refer to the first flexural cracks that develop up to the neutral axis as principal cracks.[14,51,53] Different authors use the term secondary crack to refer to different types of cracks. For example, Pérez Caldentey et al.[60] use it to denote cracks that do not reach the surface of the specimen, and others propose a distinction based on their extension over the depth of the specimen.[51,53] Brooms[14] distinguishes two types of secondary flexural cracks with different extension depending on the sequence of formation. The distinction becomes less evident in regions with variable bending moment. In this paper, the main flexural cracks are distinguished from the other cracks that have a shape tending to merge with one of the main flexural cracks.

The bond stress distribution between cracks is not uniform. Due to the propagation of conical cracks developing from the ribs that can reach the main crack,[55] bond stresses are significantly reduced near the crack. This is typically accounted for by considering a different bond–slip response near the crack[61,62] or by applying a reduction factor over a certain length.[2,21,63] Due to compatibility of displacements, the slip at the mid-point between cracks has to be zero and, therefore, bond stresses in that region are small.

Several authors have observed that the crack width at the level of the reinforcement is smaller than at the concrete surface.[58,64,65] The difference is often attributed to the secondary conical cracks.[60,64]

3 | EXPERIMENTAL PROGRAM

An experimental program was conducted in the Structural Concrete Laboratory of the École Polytechnique Fédérale de Lausanne (Switzerland) to investigate the relationship between the crack width and the stress in the reinforcement, and the development of bond stresses

in structural elements. Furthermore, results from beam tests from series SM10 by Monney et al.[5] and SC70 by Cantone et al.[33] performed in the same laboratory and instrumented with similar techniques are included in this paper.

3.1 | Tension test series TC10

3.1.1 | Main parameters and test set-up

Two tension tests were performed on reinforced concrete ties with a square cross section and a length of 1250 mm, see Figure 3a. Specimen TC11 had a cross section of 214 × 214 mm and was reinforced with 4 bars with nominal diameter (Ø) of 18 mm, as shown in Figure 3b. Specimen TC12 had a single Ø18 centered in a cross section of 100 × 100 mm. All the details including the clear cover (*c*) are provided in Table 1. The tests were performed using a Trebel Testing Machine with 5 MN capacity in

tension at a displacement rate of 0.1 mm/min. Specimen TC11 was loaded monotonically until failure. TC12 was loaded monotonically until $\sigma_{cyc,max} = 275$ MPa, then unloaded until $\sigma_{cyc,min} = 27.5$ MPa. After that, 35 cycles with the same stress range were applied before the tie was loaded until the bar yielded.

The specimens were cast horizontally, as illustrated in Figure 3c, from a single batch of normal-strength ready-mixed concrete provided by a local supplier with a maximum aggregate size of 16 mm. The compressive strength f_{cm} and the tensile strength f_{ctm} of the concrete measured on cylinders (height × diameter = 320 × 160 mm, direct tensile tests for f_{ctm}) are indicated in Table 1.

The longitudinal reinforcing bars were hot rolled high-strength threaded bars with a nominal diameter of 18 mm. As shown in Figure 3d, they had no clear yield plateau. The mean value of the yield strength at 0.2% residual strain was 731 MPa. The ribs were composed of two lugs disposed in continuous threads along the axis of the bar, see Figure 3e. They were oriented parallel to
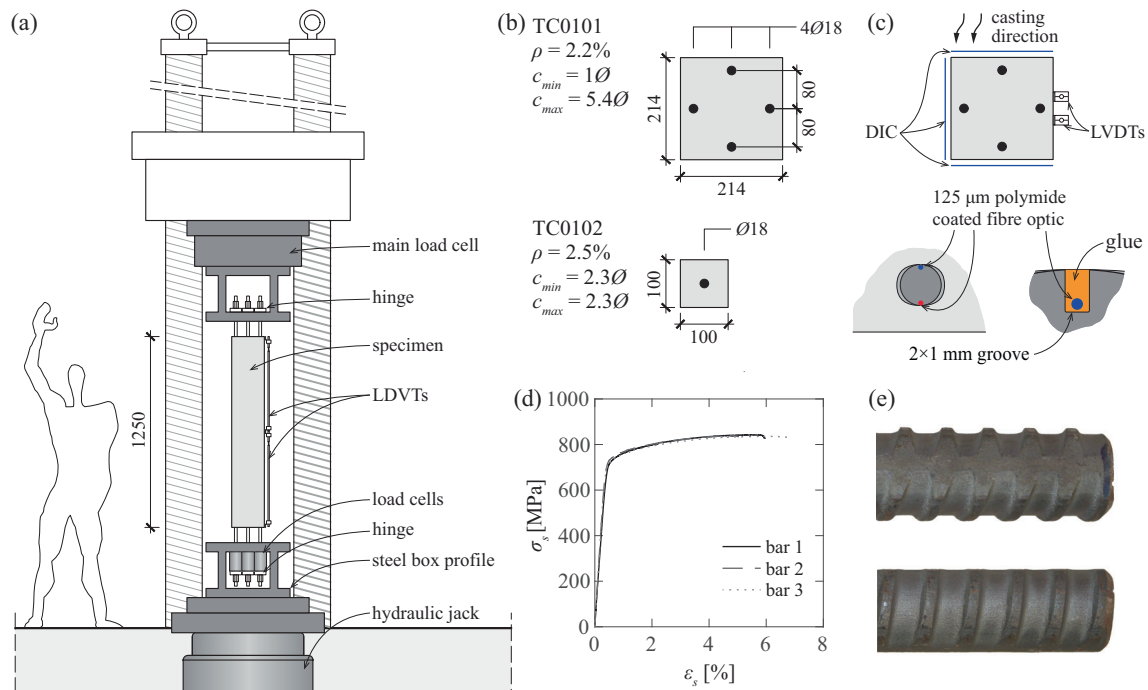

FIGURE 3 Test series TC10: (a) elevation of the test set-up; (b) specimen cross section; (c) measurement systems on the concrete surface and fiber installation for strain measurement; (d) reinforcement bar tensile tests results; and (e) rib profile.

TABLE 1 Series TC10 main parameters (see Notation for the definition of the parameters).

Specimen	Ø [mm]	Bars [−]	ρ [%]	$c/\varnothing$ [−]	Loading type	Age at testing [days]	f_{cm}[a] [MPa]	f_{ctm}[b] [MPa]
TC11	18	4	2.22	1	Monotonic	244	43.1	2.5
TC12	18	1	2.54	2.3	Cyclic	239	43.1	2.5

[a]Measured at testing age.
[b]Measured at 28 days.

the concrete surface, see Figure 3c. The geometrical characteristics of the bar were obtained from a laser scan of the surface of the bars[66]: bond index f_R 0.088, maximum rib height 1.13 mm, transverse rib angle 82°, transverse rib flank inclination 46.4° and transverse rib spacing 8.02 mm. The clear rib spacing $s_{R,clear}$ measured at the top of the lugs was 6.34 mm.

3.1.2 | Measurements

Three faces of the ties were tracked using DIC: at the bottom face of the formwork (resolution 20 megapixels and resulting pixel size 277 μm/pixel), at the top face (29 megapixels and 215 μm/pixel) and for a lateral face (5 megapixels, 544 μm/pixel), see Figure 3c. The correlation was done using VIC-3D.[67] The maximum in plane displacement error was 1/60 pixels. In the face with no DIC measurements, two LVDT's were installed to measure the total elongation.

The reinforcing bars were instrumented with Polyimide-coated optical fibers with a diameter of 125 μm running along two opposite sides of the bar, as shown in Figure 3c. A single fiber per bar was placed in grooves (1-mm wide and 2-mm deep) running along opposite faces of the bar. The fibers were oriented in a plane perpendicular to the nearest concrete surface, Figure 3c. The strains were measured using Optical Distributed Sensor

Interrogator ODiSI-6100 by Luna Innovations with a strain measurement range of ±12,000 με and a measurement accuracy of ±25 με.[68] The spatial resolution of the strain measurements was 0.65 mm, and the acquisition frequency was 10 Hz.

3.2 | Beam test series SM10

Six three-point bending tests conducted by Monney et al.[5] and one of the authors of this publication were used to characterize the cracking response of large-scale elements. Three beam specimens with constant height h of 700 mm and various widths b_w were tested as shown in Figure 4b. Each beam had two test regions with the same shear reinforcement consisting of Ø8 stirrups placed with a spacing of 200 mm, one with ductility class A and the other with ductility class C according to EC2:2004.[1] To prevent a failure in the central part, the beams were reinforced with double Ø14 stirrups with a spacing of 150 mm, see Figure 4a. The flexural reinforcement was composed of two B500C Ø34 bars ($f_{ym} = 561$ MPa) and three to six Y1050 Ø36 bars ($f_{ym} = 1014$ MPa) to provide an approximatively constant flexural reinforcement ratio ($\rho_f \sim 1.5\%$). The beams were loaded monotonically until failure using two hydraulic jacks anchored to the strong floor at a loading rate of 10 kN/min. Further details are provided in Table 2.
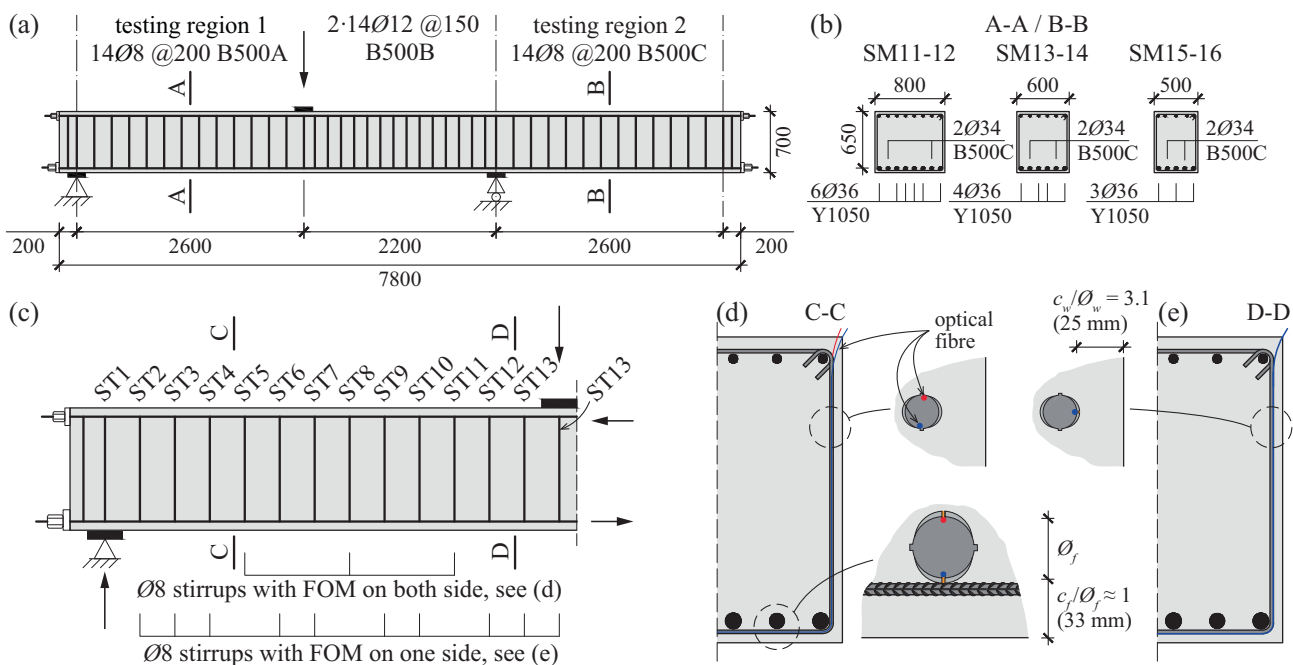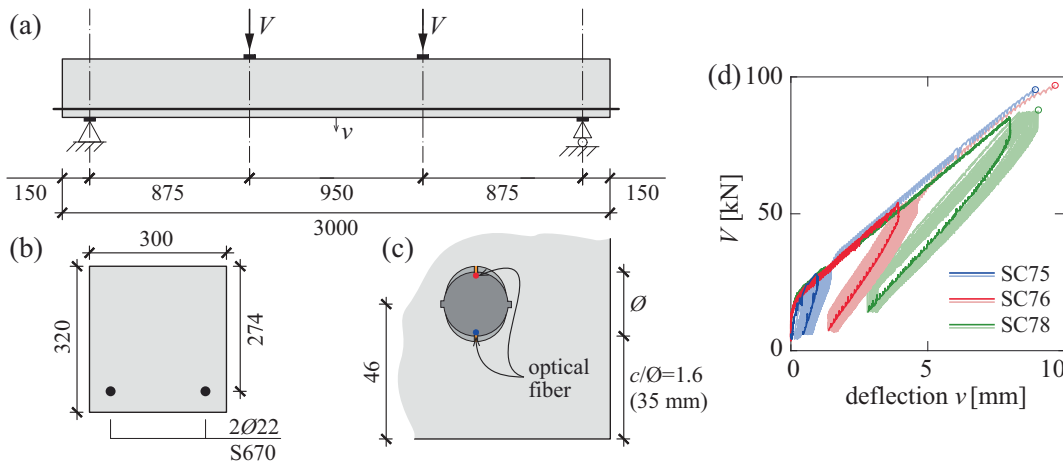

FIGURE 4 Monotonic test series SM10: (a) elevation of the test set-up; (b) cross section of the test specimens; (c) fiber instrumentation within the tested region; and details of the fiber installation in the longitudinal reinforcement and in the stirrups with (d) two sensors or (e) one sensor (for additional details, see[5]).

TABLE 2 Monotonic test series SM10 main parameters (see Notation for the definition of the parameters).

Test	Shear reinf. ductility class	b_w [mm]	h [mm]	ρ_f [%]	ρ_w [%]	f_{cm} [MPa]	f_{ctm} [MPa]	f_{ywm} [MPa]	V_{max}[a] [kN]
SM11	A	800	700	1.52	0.063	50.7	3.2	505	603
SM12	C	800	700	1.52	0.063	50.6	3.2	538	610
SM13	A	600	700	1.51	0.084	50.4	3.2	505	540
SM14	C	600	700	1.51	0.084	50.4	3.1	538	639
SM15	A	500	700	1.50	0.101	50.2	3.1	505	454
SM16	C	500	700	1.50	0.101	50.0	3.1	538	515

[a]Measured shear strength without self-weight.

FIGURE 5 Cyclic test series SC70: (a) elevation of the test set-up; (b) cross section of the specimens; (c) fiber instrumentation within the tested region; and (d) applied shear as a function of the mid-span deflection for specimens SC75, SC76 and SC77 (for additional details, see[33]).

With an effective depth d of 650 mm, the nominal clear cover c_f of the flexural reinforcement was 33 mm ($\sim 1\varnothing_f$), while the nominal clear cover c_w for the stirrups was 25 mm ($3.1\varnothing_w$) as shown in Figure 4d. The Ø34 bars had a bond index of 0.052 and a clear rib spacing of 16.3 mm. The Ø8 type A bars had a bond index of 0.047 and a clear rib spacing of 4.5 mm. The Ø8 type C bars had a bond index of 0.069 and a clear rib spacing of 5.1 mm.

The two lateral faces were tracked with DIC. In each beam, the two longitudinal Ø34 bars were instrumented with a single fiber optic installed along two opposite sides of the bar, as illustrated in Figure 4d. The 125 μm polyimide-coated fibers were placed in a groove 2 mm deep in the longitudinal reinforcement and 1 mm deep in the stirrups. The stirrups ST2 to 13 were instrumented with fibers, as shown Figure 4c. Stirrups ST5, 8 and 11 had one fiber running along the opposite faces of the stirrup, see Figure 4d. The rest had only one fiber running along the perimeter of the stirrup, see Figure 4e. For additional details, see Monney et al.[5]

3.3 | Beam test series SC70

Three four-point bending tests conducted by Cantone et al.[33] were analyzed to characterize the cracking response under cyclic loading. Figure 5a shows the main dimensions of the test set-up. The beams had a height of 320 mm, a width of 300 mm and a longitudinal reinforcement consisting of two high-strength Ø22 bars, see Figure 5b. The effective depth was 274 mm, leading to a nominal clear cover c_f of 35 mm ($1.6\varnothing_f$), see Figure 5c. No shear reinforcement was disposed.

The beams were loaded cyclically with three different shear force ranges. SC75 was loaded up to a maximum shear correspondent to the theoretical cracking force. SC76 was loaded up to a shear force of 55% of the shear strength V_{max}. SC77 was loaded up to the formation of the sub-horizontal branch of the shear crack. After 50 cycles, the specimens were loaded until failure, except for specimen SC77 where the propagation of the shear crack due to cyclic loading led to a premature failure after 21 cycles. The main parameters of the tests are given

TABLE 3 Cyclic test series SC70 main parameters (see Notation for the definition of the parameters).

Specimen	b_w [mm]	h [mm]	ρ_f [%]	ρ_w [%]	f_{cm} [MPa]	f_{ym} [MPa]	Cycles [−]	$V_{cyc,min}$ [kN]	$V_{cyc,max}$ [kN]	V_{max}[a] [kN]
SC75	300	320	0.92	–	33.3	701	60	27.8	5.3	95.4
SC76	300	320	0.92	–	36.0	701	50	54.0	7.3	97.1
SC77	300	320	0.92	–	36.3	701	21	86.4	10.2	80.7

[a]Shear strength including self-weight.

in Table 3. Figure 5d shows the shear force as a function of the mid-span deflection for the three tests.

The front face of the specimen was tracked with DIC. In each beam, the longitudinal Ø22 bar closest to the front face was instrumented with a single optical fiber installed in a 2 mm deep groove running along two opposite sides of the bar, as shown in Figure 5c. For additional details, see Cantone et al.[33]

3.4 | Measurement postprocessing

The DIC results were used to detect the crack patterns and to estimate crack kinematics using the Automated Crack Detection and Crack Measurement (ACDM) procedure developed by Gehri et al.[69] Consequently, the measured crack widths correspond to the values at the level of the reinforcement and on the surface of the concrete.

The fiber strain measurements were postprocessed to remove noise and the large variations due to the variable cross section and the introduction of bond stresses at the ribs.[33,70,71] For this purpose, a moving average filter over a length of two bar diameters was used. The bar strains are calculated by averaging the results from the two sides of the bar. The stresses are calculated assuming a bilinear stress–strain constitutive law assuming an elastic modulus of $E_s = 200$ GPa and a strain hardening modulus according to the respective tensile tests. Local bond stresses (τ_b) are derived from the equilibrium considerations of a finite bar element[33] only in the elastic range of the bar. Average bond stresses ($\tau_{b,avg}$) are computed based on the average of the local bond stresses over the relevant length. The curvature of the bar (χ_s) is calculated assuming a distance between fibers equal to the nominal bar diameter minus 4 mm, assuming that the fiber is at the bottom of the groove.

The slip considered for the estimation of the local bond–slip response is estimated from the steel strains measured with the fibers. The steel strains are integrated from the point where strains where negligible (point at approximately l_{cr} from the crack) during the crack formation phase, or from the inflection point of the strain profiles (similar to the mid-point between cracks) during the stabilized cracking stage. The cracking sequence is considered and concrete strains are neglected.

4 | EXPERIMENTAL RESULTS AND DISCUSSION

4.1 | Tensile tests

The results of the tension test series TC10 are presented in Figure 6. The relationship between average stress in the reinforcement (calculated as the applied force divided by the nominal steel area) and the average strain (calculated as the average of the fiber measurements divided by the tie length, namely 1250 mm) is shown in Figure 6a. For each specimen, the measured response (including the initial shrinkage strains) is shown with a black solid line and the bar tensile tests (gray hatch) are shown. The response after removing the initial shrinkage strains (black dashed line) is shown for visual reference. The initial shrinkage strains were around −0.14‰ and −0.25‰ for specimens TC11 and TC12, respectively. These results are in the same order of magnitude as those found in the literature.[35,39] Furthermore, the difference between them is probably related to the different ratio between the element cross section and its perimeter (often referred to as notional size in standards,[2] 107 and 50 mm for specimens TC11 and TC12, respectively). Elements with smaller ratios have a larger specific surface and therefore a faster drying shrinkage, in this case TC12.

Figure 6b,c shows the crack patterns for the North and South faces of specimen TC11 at two load steps. The two faces correspond respectively to the bottom and the top faces during casting. Due to the relatively small cover, several non-traversing cracks originating from the conical cracks at the ribs[55] are visible. Some of them eventually propagated to become traversing cracks. The figures show the steel strain ε_s, the axial stress σ_s (calculated form the strains with the assumed stress–strain relationship) and the bond stress τ_b distributions for 6 load steps along the tie. The strain and stress profiles show good correlation with the crack patterns. The traversing cracks lead to peaks in the distributions, whereas the
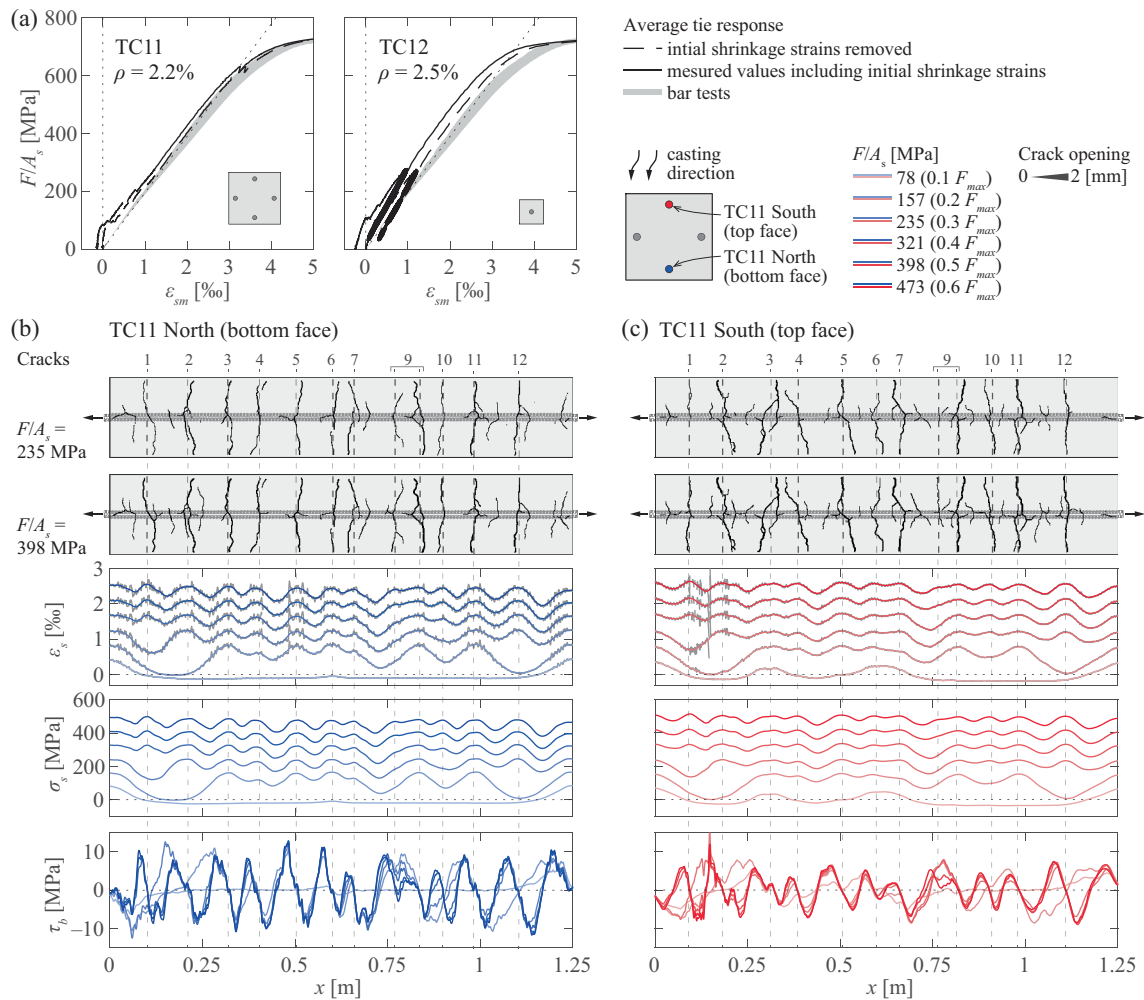
FIGURE 6 TC10 series main results: (a) steel average stress–strain diagrams for specimens TC11 and TC12; and crack patterns, steel strain, steel stress and bond stress distributions along the bonded lengths for the (b) North face and (c) South face of specimen TC11 (corresponding to good and poor casting conditions respectively, see sketch in the top right part of the figure).

non-traversing cracks lead to flatter stress distributions near the crack. This indicates that the conical cracks are probably consequence of the incompatibility of deformations between the steel and the concrete, and that the slip occurs in the same direction as in the crack. Consequently, the considered crack spacing is the spacing between traversing cracks. The average crack spacings are 102 and 105 mm for the North and South faces of specimen TC11 and 131 mm for specimen TC12 (similar values for both faces).

The stress distributions near the crack location and the point between cracks vary smoothly, indicating low bond stresses. This can also be observed in the bond stress distributions. Smaller bond stresses are developed for the bar at the top of the formwork. This is a well-known effect due to the plastic settlement and bleeding voids that form under the bars.[45,72,73] However, it is surprising to see this effect considering that the depth of the specimen TC11 is 214 mm and, consequently, both bars

are in good casting conditions according to current standards.[1,2,47]

The results of the DIC and fiber optical measurements provide detailed information of each crack with a precision that outperforms conventional measurement techniques. Figure 7a shows the contribution of the different cracks to the total crack width (w) of crack 2 of the bottom face of specimen TC11 (TC11 North). It can be observed that the width at the initial traversing crack (point A) does not increase after a stress of around 300 MPa. After that, a second and a third crack develop (points B and C), that concentrate additional components of the crack width. At a larger stress level, another non-traversing crack develops (point D) with a negligible contribution ($w \approx 0.01$ mm). The total crack width measured at the concrete surface near the bar is smaller than the corresponding width near the corners of the specimen (points E and W). This is consistent with experimental measurements that show the variation of the crack with
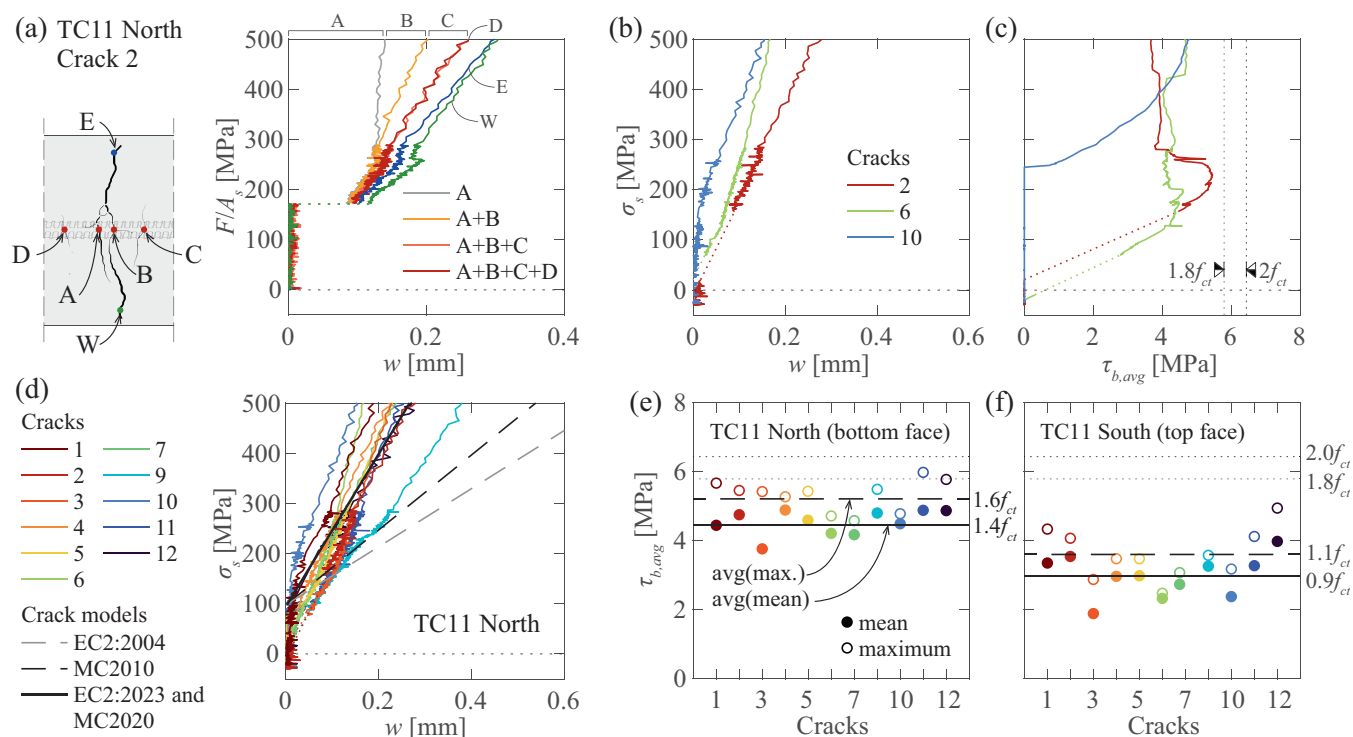
FIGURE 7 Detailed crack results from specimen TC11: (a) contributions of the secondary cracks to the crack width of crack 2 on the North face (see Figure 6b); (b) bar stress–crack width and (c) bar stress–average bond stress diagrams for selected cracks on the North face; (d) bar stress–crack width diagrams for all cracks on the North face; and mean and maximum values of the average bond stress on both sides of the crack (in the range between $w \geq 0.1$ mm and $\sigma_s < 500$ MPa) for (e) bottom face (North), and (f) top face (South).

over the concrete cover.[64,74] It indicates that the crack width at the bar location is likely smaller than the crack width observed on the concrete surface, particularly for large covers. For this reason, the calculated crack widths in this paper include the neighboring secondary cracks if present.

The bar stress (estimated from the fiber measurements) as a function of the crack width is shown in Figure 7b for some cracks on the bottom face of specimen TC11. Using the bond stress distributions from Figure 6b, c, the average bond stress at both sides of the crack (spanning between the mid-points between the studied crack and the adjacent cracks) can be calculated for each load step. Figure 7c shows the average bond stress as a function of the steel stress in the bar. Two cases can be observed: for crack 10 (which was a secondary crack that eventually propagated across the full section), the bond stress tends to increase with increasing steel stress and crack width; whereas in the case of cracks 2 and 6 (which developed earlier as principal cracks) the average bond stress undergoes sudden variations. These variations occur when principal or secondary cracks develop. This can be understood by looking at the bond stress diagrams in Figure 6b. The distribution changes significantly before and after the development of cracks 1 and 2, which

explains how the average bond on the left side of crack 3 can vary. Similar changes were observed by Cantone et al.[33]

Figure 7d shows the bar stress – crack width relationships for all the cracks on the bottom face TC11. In general, the results show rather linear trends as predicted by the stabilized crack model presented in Section 2.1. Some cracks show some trend variations, for example crack 6 (Figure 7b). This could be due to the residual tensile strength of concrete, given the small crack widths, or due to the fact that crack 6 did not fully propagate initially, as can be observed in Figure 6c. The figure includes the design crack width formulations based on the maximum crack spacing according to EC2:2004 ($s_{cr} = 336$ mm for $c = 18$ mm, dashed gray line) and MC2010 ($s_{cr} = 261$ mm for $c = 18$ mm, dashed black line). The maximum spacings are larger than the average measured value. This is reasonable since the length of the tie is relatively short, therefore the maximum crack spacing is unlikely to occur. These results agree with the tendency of the formulation in EC2:2004 to overestimate the crack spacing reported by Pérez Caldentey et al.[45] The formulations of EC2:2023 and MC2020 lead to a mean calculated crack spacing of 125 mm (for $c = 18$ mm), which corresponds well to the measured values (black solid line). If

the maximum cover is considered ($c = 98$ mm), the calculated maximum spacings according EC2:2004 (608 mm) and MC2010 (323 mm) and the calculated mean spacing according to the EC2:2023 and MC2020 (245 mm) are larger than the measured values.

Figure 7e,f shows the average bond stress in the range with $w \geq 0.1$ mm and $\sigma_s < 500$ MPa for each crack. Two values are presented: the mean value within the range (solid circular markers) and the maximum value in the range (empty circular marker). It can be observed that both values are below the values proposed by the codes. Furthermore, the values of the top face (Figure 7f) correspond to approximately 65% of the values of the bottom face (Figure 7e). This value is close to the factor typically assumed for design anchorage lengths in poor casting conditions ($\eta_2 = 0.7$)[1,2] and to the recently proposed factor of 0.75 for the crack width calculation.[44]

4.2 | Monotonic beam tests

Figure 8a shows the crack pattern obtained from the DIC strain field at 90% of the maximum load for the North face of specimen SM15 (the width of the black lines is proportional to the crack width). The shear failure crack can be easily identified. It can also be observed that most of the flexural cracks occur at the location of the stirrups. In this case, the transverse reinforcement cannot provide confinement for the bond developed between the cracks.

Figure 8b shows the results of the fiber measurements including the measured steel strain, the calculated bond stress and the normalized curvature in the bar $\chi_s \cdot \varnothing/2$ (strain in the bar related to local bending due to dowel action and other effects[33]). A good agreement between the strain peaks and the crack positions can be observed. The strains calculated assuming an elastic cracked response of the section (lever arm $z = d - h_c/3$, h_c being the depth of the compression zone assuming a linear elastic behavior of concrete, neglecting the residual tensile strength of concrete after cracking and not considering the effect of the shear force) are indicated with a dashed line. The corresponding calculated stresses are smaller than the values derived from fiber measurements, as consistently observed in specimens subjected to shear.[33,75] This can be explained by the inclination of the cracks (the bending moment should be calculated at the tip of the crack and accounting for the force in the stirrups).[33] For shear forces closer to the shear strength, the propagation of the delamination crack due to dowel action in the flexural reinforcement[50] leads to a
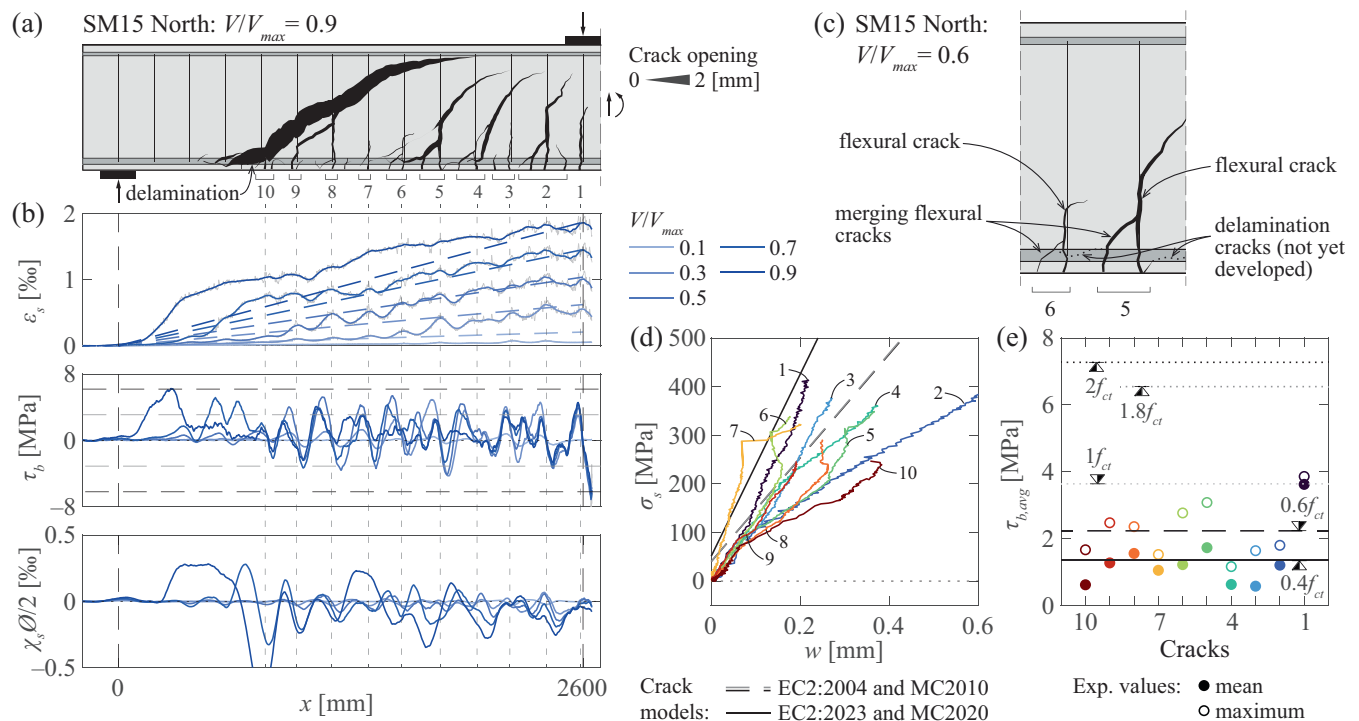

FIGURE 8 Detailed crack results of the flexural reinforcement from the North face of specimen SM15: (a) crack pattern for $V/V_{max} = 0.9$; (b) steel strain, bond stress and normalized curvature distributions for five load levels; (c) contribution of the secondary cracks to the crack width for cracks 5 and 6; (d) bar stress–crack width diagrams for all cracks; and (e) mean and maximum values of the average bond stress at both sides of the crack (in the range between $w \geq 0.1$ mm and $\sigma_s < 500$ MPa).

considerable increase in the strains and stresses in the reinforcement in that region.[33,76]

The bond stress profiles in the longitudinal reinforcement presented in Figure 8b have the same appearance as in the ties; however, notably smaller values are observed, even though the concrete strength was higher in the beam tests. The curvature profiles show that significant local bending occurs in the bars, particularly as the delamination crack develops. This bending can significantly increase the maximum stress at the surface of the bar. At the same time, stress concentrations occur in that region due to the introduction of the bond stresses.[33,59] This can have a negative effect on the fatigue resistance as the ribs are known to cause stress concentrations leading to the initiation of fatigue cracks.[77,78]

Tests in reinforced concrete beams have shown that the fatigue resistance of reinforcing bars is lower than that of bare bars.[79] In regions subjected to bending, the maximum axial stress at the surface of the bar might occur at the crack location due the axial force and the local curvature of the bar. In regions subjected to bending and shear (more common in structural elements), the maximum is not necessarily at the location of the crack due to dowel action. The stress concentrations induced by the bar-to-concrete interaction will occur somewhere within the concrete between cracks as shown by the bond profiles. Further research is required to determine which of the two effects has a bigger influence on the fatigue resistance of the bar.

The bar stress as a function of the crack width is shown in Figure 8d. As explained in the previous section, neighboring cracks can concentrate part of the total crack width. In most of the flexural cracks, another flexural crack developed and merged in the lower part of the beam as shown in Figure 8c.[50] Both crack widths at the level of the reinforcement are considered. The curves also show a fairly linear response in most cases with a larger slope, which is consistent with the larger crack spacings according to Section 2.1. In this case, the average experimental crack spacing (206 mm) is similar to the maximum crack spacing according to EC2:2004 (186 mm) and MC2010 (187 mm). Agreement between EC2:2004 and MC2010 in the crack spacing shows that EC2:2004 is better calibrated for flexural tests. The mean calculated spacing according to EC2:2023 and MC2020 is 107 mm. Some of the experimental curves show sudden trend changes for large stresses (near the shear capacity of the specimen). This is probably related to the propagation of several small delamination cracks at the bottom of the specimen (see Figure 8a) that cross the other cracks, disturbing the DIC results in the points considered for the crack kinematic calculation. The average bond stress results for all the cracks presented in Figure 8e confirm

the extremely low bond stresses (around $0.5f_{ct}$) compared with code formulations. Similar values were obtained for the other specimens of the series. This can be explained by the large diameter of the bars, the small cover of the longitudinal bars, the small spacing between bars and the development of splitting cracks along the bars (visible in the bottom face of the specimens). The effect of these parameters, which are not accounted for in current crack formulations, will be discussed in the following.

Figure 9a,b shows the crack patterns and the stress profiles of the stirrups from specimens SM13 and 14. The stress profiles show the occurrence of peaks at the crack locations, leading to the yielding (red lines) in some stirrups close to the maxim load (shear strength). In most cases, the fiber measurements were lost soon after yielding (regions without measurements in the figure).

Based on the stress distribution, the average bond stresses were calculated for crack points that were not too close to the bends of the stirrup (see Figure 4e) where only a single crack was traversing the stirrup. The average stress was computed for the maximum load (solid marker) or before yielding of the reinforcement (empty marker), if this occurred before the maximum load. Therefore, the average bond stresses were not calculated when the signal was lost, which was typically the case after yielding. The results presented in Figure 9c,d show that two cases can be distinguished: stirrups activated by an inclined crack (blue and red markers for the top and bottom parts respectively, see sketch in Figure 9d) and stirrups where besides the inclined crack, a flexural crack developed creating a longitudinal crack along the stirrup (green and yellow markers for the top and bottom parts respectively). The results show that the average bond stresses are generally smaller for the stirrups that did not reach yielding. The results also indicate that the regions affected by the longitudinal cracks along the stirrups have lower average bond stresses. This can be explained because the inclined cracks in these regions have typically smaller openings (compared with the stirrups that yielded) and because of the reduction of the contact area between the ribs and the concrete due to the crack development.[25,80] Similar results were found in the other specimens. In most cases, for the bars that yielded, the average bond stresses just before yielding reach values close or larger than the proposed values of current codes. The values for the bars that did not yield were lower.

4.3 | Cyclic beam tests

Figure 10a,b shows the crack patterns and fiber measurement results for specimens SC75 (maximum load reaching the cracking load) and SC77 (maximum load
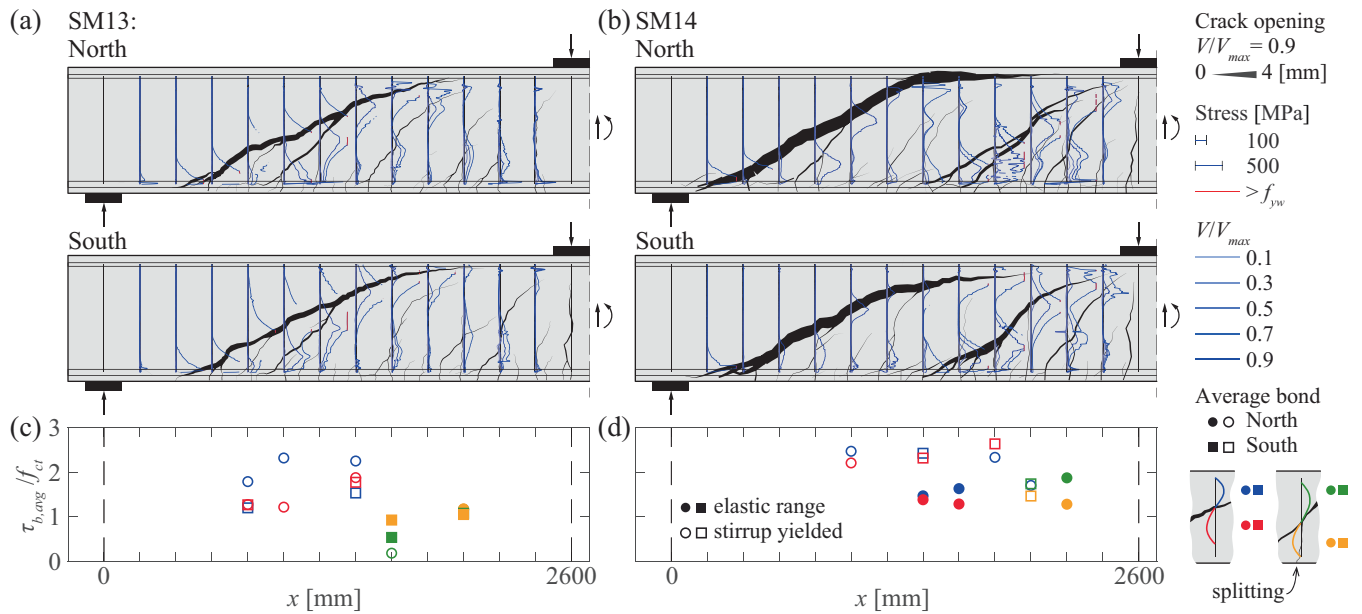
FIGURE 9 Detailed crack results of the stirrups: (a and b) crack pattern at $V/V_{max} = 0.9$ and stirrup stress distributions for five load steps; and (c and d) average bond stress (at V_{max} or before yielding of the stirrup) for specimens (a and c) SM13 and (b and d) SM14.
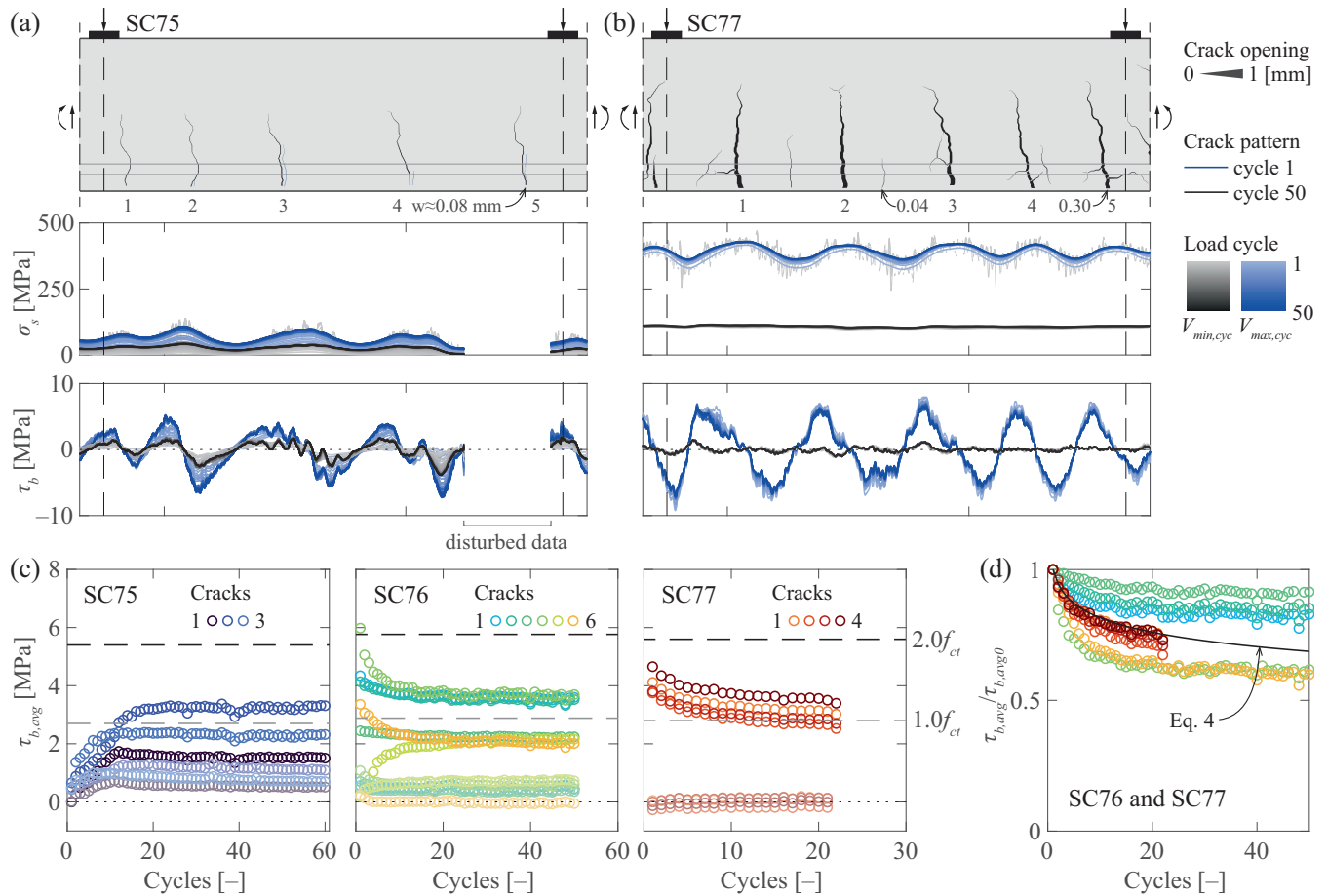

FIGURE 10 Detailed crack results of the flexural reinforcement from series SC70: crack pattern at maximum load, steel strain and bond stress distributions for all cycles for specimens (a) SC75 and (b) 77; (c) average bond stress as a function of the number of cycles for specimens SC75, 76 and 77; and (d) relative reduction of the average bond stresses with the number of cycles.

reaching $0.9V_{max}$), respectively. For specimen SC75, peaks in the steel stresses in the longitudinal bars can be observed at the crack locations since the first cycle. However, not all the cracks could be detected with the DIC measurements (this is perhaps related to the fact that nonlinear concrete strains in tension can appear before reaching the tensile strength and the development of cracks[81,82]). In Figure 10a, the crack pattern for the first cycle is shown in blue (shifted to the right for clarity) and for the last cycle is shown in black. Cracks 2 and 4 did not extend beyond the reinforcement position at the 1st cycle, and cracks 3 and 5 reached only half of their final length with widths of around 0.03 mm. For specimen SC77, all the cracks were present since the first cycle and only a slight increase in the width and small propagations of some secondary cracks were observed. The bond stress distributions at $V_{max,cyc}$ indicate that bond stresses increase with the cycles in specimen SC75 and decrease for SC77.

This is more evident in the results presented in Figure 10c, that show the evolution of the average bond stress over the cycles. The difference can be explained by the fact that in SC75, the increase of crack width is mostly related to a propagation of the crack in the zone with residual tensile strength under the neutral axis and a reduction of the uncracked zone, which leads to an increase of the tensile stress in the reinforcement and an increase of the bond stresses. For specimen SC77, the crack development is very small and the decrease of the bond is due to the load cycles that deteriorate the interface as observed by other researchers.[33,35]

As shown in Figure 10c, the steepest variations occur in the first 10 to 15 cycles. At the end of the cyclic loading, the bond stresses remain fairly stable for SC75. For SC76 and SC77 a slight decreasing trend remains after the applied cycles, particularly in SC77. Bond stresses increase with the cycles in crack 5 of SC76, this is because the crack propagated from a small crack in the first cycles. No clear trend regarding the average bond stress and the presence or absence of splitting and secondary cracks can be observed. It must be noted that the bond stresses are in all cases lower than the values proposed by the codes. At $V_{min,cyc}$, the variations are considerably smaller.

Figure 10d shows the relative reduction of average bond stresses at $V_{max,cyc}$ compared with the value correspondent to the first cycle ($\tau_{b,avg0}$), in agreement with previous research.[33,35,83,84] The general trend is well captured by the reduction factor proposed by Lemcherreq et al.[35] defined by Equation (4).

$$k_{cyc} = 1 - 0.08 \log N. \tag{4}$$

5 | IMPROVEMENT OF THE BOND–SLIP RELATIONSHIP

Considering that the underlying mechanisms of the bond response of anchorages and near cracks are the same, the local bond–slip relationship can be used to determine the bond in service conditions. A clear difference between both phenomena is the range of slips. In a cracked element, due to compatibility conditions, the mid-point between cracks cannot slip. At the same time, near the crack (if the influence of the secondary cracks is neglected), the slip should correspond to half of the crack width. This yields maximum slips in service conditions of around 0.1–0.3 mm.

Another significant difference, particularly for relatively small crack spacings, is that the influence of the secondary cracks and the resulting reduction of bond near the crack is not negligible. Debernardi et al.[85] adapted the model proposed by Balázs[20] to account for the loss of bond near the loaded area, establishing that the average bond should remain constant. However, recent experimental results from ties and beam tests show that average bond increases with the load in monotonic tests.[34,36]

The authors recently proposed a bond–slip relationship based on mechanical considerations that shows good agreement with the results of a large test database.[40] The relationship depends on the confinement provided by the concrete cover and the transverse reinforcement. As explained in Section 4.2, the confinement provided by the stirrups is not considered in this case, due fact that most of the flexural cracks appeared at the stirrup locations. Figure 11a shows the general formulation for each segment of the curve and the resulting bond–slip law for good casting conditions and three concrete covers. The largest bond stresses are reached for well-confined conditions ($c/\emptyset \geq 5$); and lowest for unconfined conditions ($c/\emptyset \leq 1$). Intermediate cases are considered as moderately-confined conditions. More details are provided in Appendix B.

The ascending branch is controlled by the pull-out bond stress ($\tau_{bu,po}$) and the peak bond slip ($\delta_{sc1,po}$) in well-confined conditions that depend on the concrete compressive strength, the bar diameter and the bond index, as described in Equations (5) and (6).

$$\tau_{bu,po} = 0.5 f_{cm} \left(\frac{30}{f_{cm}}\right)^{1/6} \left(\frac{20}{\emptyset}\right)^{1/8}, \tag{5}$$

$$\delta_{sc1,po} = 1.0 \cdot \frac{\emptyset}{20} \cdot \left(\frac{30}{f_{cm}}\right)^{1/3} \left(\frac{0.08}{f_R}\right)^{1/5}. \tag{6}$$
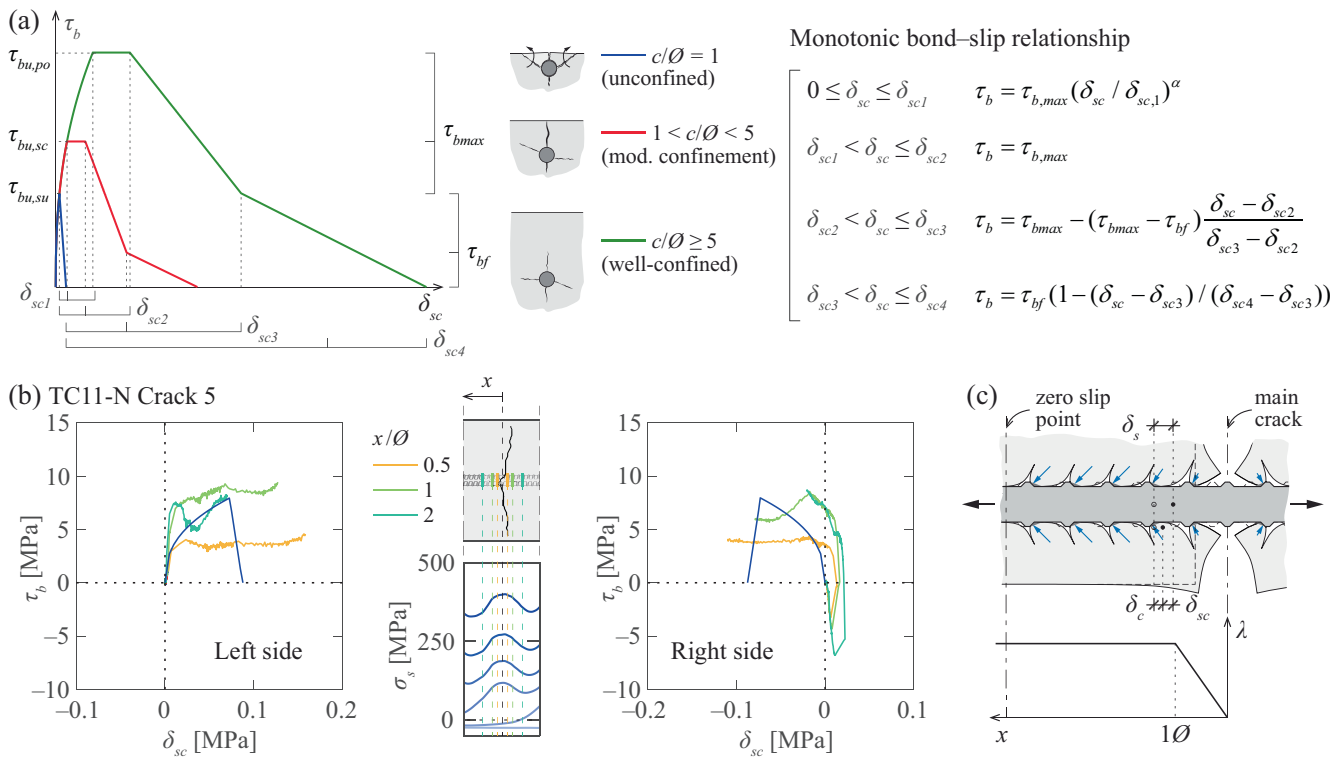
FIGURE 11 Local bond–slip response: (a) considered local bond–slip response for monotonic loading; (b) local bond–slip measurements on both sides of crack 5 of the North face of TC11; and (c) proposed reduction factor for the bond stress near the crack.

Figure 11b shows the local bond–slip relationship at distances of 0.5, 1 and 2Ø from crack 5 of the North face of specimen TC11, obtained from the fiber optical measurements. The cracking sequence was considered to estimate the slip, which explains the results in the right side of the crack where slip and bond stresses initially develop in the opposite direction. The proposed relationship (blue curve) follows the general trend of the experimental results at 1 and 2Ø from the crack; however, the initial stiffness is slightly underestimated. The measurements show a reduction of the bond stresses at 0.5Ø from the crack. Consequently, a linear bond reduction factor (λ) acting over a distance of 1Ø from the crack is considered, as shown in Figure 11c.

Using the proposed bond–slip relationship (Figure 12a) and reduction factor to account for secondary cracks (Figure 11c), a numerical integration was performed as proposed by Balázs.[20] The results in terms of the average bond stress as a function of the crack width are illustrated in Figure 12b–d for Ø8, Ø18 and Ø34 bars. The colors correspond to different confinements. For each crack spacing (curves with different color shades), the average bond stress before yielding of the reinforcement is represented with a solid line and the yielding point with a circular marker. The favorable effect of the confinement and the size effect are clearly visible in Figure 12b–d.

The response in well-confined conditions (sufficient cover) is governed mostly by the ascending branch. In these conditions, the average bond stress can be estimated using Equation (7) (dashed curve in Figure 12b–d). This expression is derived using the analytical solution for the average bond stress as a function of the crack width in homogeneous conditions, multiplied by an adjustment factor k_{sr} depending on the crack spacing (a constant value of 1.3 is proposed):

$$\tau_{b,avg} = k_{sr} \cdot \tau_{b,max} \frac{1-\alpha}{1+\alpha} \left(\frac{w}{2 \cdot \delta_{sc1}} \right)^{\alpha}, \qquad (7)$$

where α is the exponent of the ascending branch of the local bond–slip relationship (a value of 0.4 as proposed in MC2010 is considered). Equation (7) is valid for bars in good bond conditions and without the development of splitting/spalling cracks along the reinforcement bar.[25] The improvements of Equation (7) to account for other effects are described in the following paragraphs.

As observed by Moccia et al.,[73] the bond performance of bars is influenced by the plastic settlement voids and cracks. The effect is directly related to the height of the bar above the formwork. In this paper, only results from one relatively shallow specimen are available. Based on these results, the factor of $\eta_2 = 0.7$, typically considered for short anchorages, seems to give a good estimation of
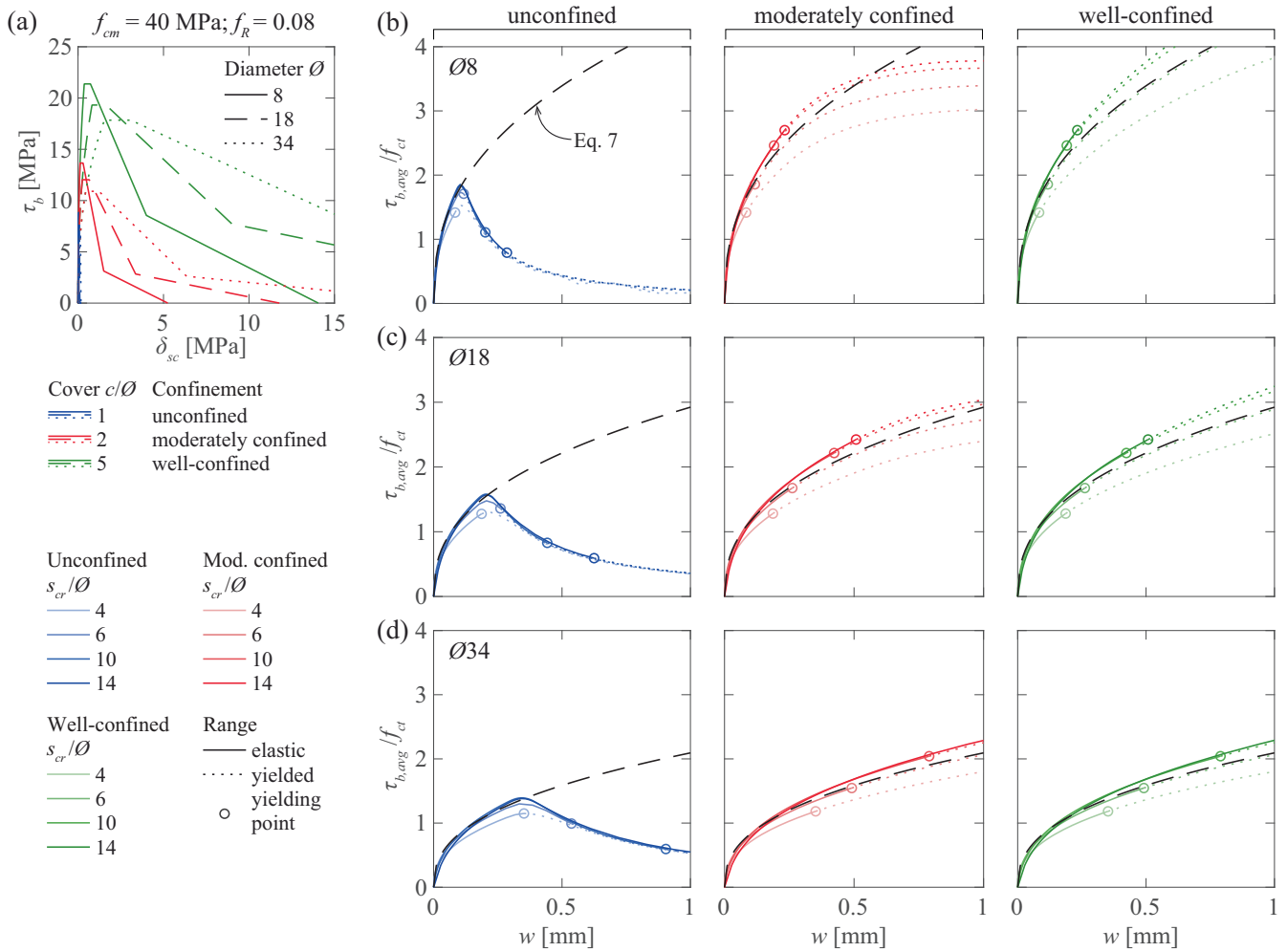
FIGURE 12   Bond in the stabilized cracking phase: (a) considered local bond–slip relationships; and average bond stress as a function of the crack width for (b) Ø8, (c) Ø18, and (d) Ø34 bars.

the bond stress reduction. Further, research is needed to confirm these results.

Based on the work of Brantschen et al.,[80] the authors recently showed that the development of local bond stresses along the anchorage length is affected by the development of splitting and spalling cracks along the bar due to the reduction of the contact surface between the ribs and the concrete.[25] Using as reference the bond–slip relationship for well-confined conditions, the local bond stresses can be determined using a reduction factor based on the splitting and spalling crack widths. Consequently, the integration of the different local bond–slip relationships (shown in Figure 12b–d) inherently accounts for the splitting and spalling crack development. However, as Equation (7) accounts for the ascending branch and the conical cracks, the effects of splitting are not considered. In existing structures, the splitting cracks can be measured. Furthermore, longitudinal cracks along the reinforcement can appear for other reasons (such as the flexural cracks along the stirrups

shown in Figure 9a,b). Consequently, the factor proposed by Brantschen et al.[80] defined by Equation (8) can be adopted as a reduction factor for cases where cracks along the reinforcement bar are observed on the concrete surface.

$$k_{lc} = \frac{\tau_b}{\tau_{b0}} = \frac{1}{1 + \frac{\kappa_f}{f_R}\frac{w_{lc}}{\varnothing}},$$ (8)

where κ_f is a factor proportional to the number of lugs composing the ribs ($\kappa_f = 0.75n_l$) and w_{lc} is the width of the longitudinal crack along the reinforcement. If the rib geometry information is not available, the value corresponding to two rib lugs ($\kappa_f = 1.5$) and a bond index of 0.08 (average value from the database used for the derivation of the bond–slip relationship[40]) are recommended.

Considering these two factors and the cyclic reduction factor of Equation (4), the expression to estimate the bond stresses is defined by Equation (9):

$$\tau_{b,avg} = \eta_2 \cdot k_{sr} \cdot k_{lc} \cdot k_{cyc} \cdot \tau_{b,max} \frac{1-\alpha}{1+\alpha} \left(\frac{w}{2 \cdot \delta_{sc1}} \right)^{\alpha}. \quad (9)$$

After yielding, the bond stresses reduce significantly.[29,63,86] This is out of the scope of this paper, especially as in such case, the stress in the bar is less uncertain.

6 | COMPARISON OF THE PROPOSED MODEL WITH THE EXPERIMENTAL RESULTS

6.1 | Average bond stresses

Figure 13a shows the experimental results (colored lines) and the proposed analytical expression (dashed black line) in terms of the average bond stress as a function of the crack width. Additionally, the results of the numerical integration of the local bond–slip relationships are shown with a gray hatch. The increase of the bond stresses with the crack width is well captured. However, stresses are slightly underestimated. Figure 13b shows the mean (filled marker) and maximum values (empty marker) of the average bond stresses for the flexural

reinforcement of all specimens of series SM10. The corresponding predicted values are shown with black markers. The size effect and the influence of the longitudinal cracks along the bars reduce considerably the bond stresses. Nevertheless, the proposed values overestimate the experimental ones by a factor close to 2. This overestimation is likely due to the fact that the widths of the delamination cracks in the lateral faces of the specimen are smaller than in the middle of the specimen due to the presence of the stirrups. The values proposed by the codes (1.8 to $2f_{ct}$) overestimate experimental results by a factor of 3 to 4.

Figure 13c shows the results from the stirrups not affected by the presence of cracks along the bars (flexural cracks), as explained in the previous section (see Figure 13e). The average bond stresses are slightly overestimated, particularly for the B500A stirrups (Figure 13c). This can be explained by the lower bond index of the bars and could indicate that the influence of this parameter in the proposed bond–slip relationship is underestimated. These results are coherent with the smaller crack spacings for larger bond indices observed by Galkovski et al.[34] Figure 13d shows the results from the stirrups affected by the flexural cracks. In general, the influence of splitting is satisfactorily considered by the splitting factor (triangular black markers). Additional experimental data is required
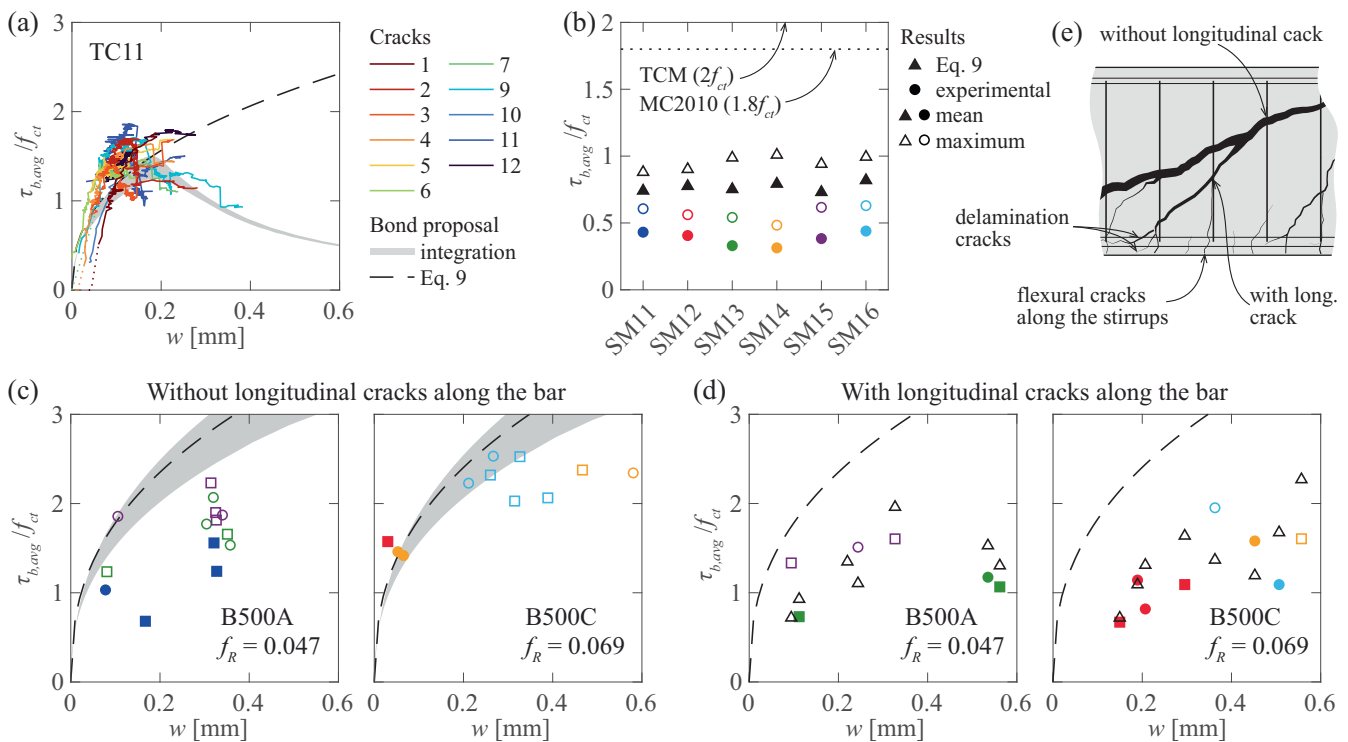

FIGURE 13 Comparison of the proposed average bond stresses and the experimental values: (a) specimen TC11; (b) flexural reinforcement of series SM10; (c) shear reinforcement without and (d) with cracks along the bar; and (e) schematic representation of stirrups with and without cracks along the bars.

to improve the estimation of this effect, particularly for small diameters.

6.2 | Steel stress estimation based on the crack width

Three estimations are compared with the experimental values and, in all three cases, the measured shrinkage strains are included in the relative mean strain calculation:

- Using the proposed model for the crack width estimation (Equations 3 and 9) and the measured crack spacing (distance between mid-points of consecutive cracks measured from the DIC).
- Using the relative mean strain according to EC2:2004 and the measured crack spacing. It must be noted that the relative mean strain is the same according to MC2010.

- Using the relative mean strain according to EC2:2023 and the measured crack spacing. It must be noted that the relative mean strain is the same according to MC2020.

Figure 14a shows the ratio of experimental over calculated stresses for tie TC11. The results indicate that the proposed model slightly underestimates the stress in the bar. This can be explained by the underestimation of the bond stresses (see Figure 13a). The code formulation slightly overestimates the stress. As explained in Section 2.1, for a given crack spacing and width, the code estimation yields larger bar stresses (see Figure 2a). Consequently, the code formulation tends to overestimate the stresses. Figure 14b shows the results for the flexural reinforcement of the beams from series SM10. The proposed model performs better than the code formulation for small crack widths. This is due to the bond activation expression, that gives a good estimation of the average bond stresses for smaller crack widths. For larger crack
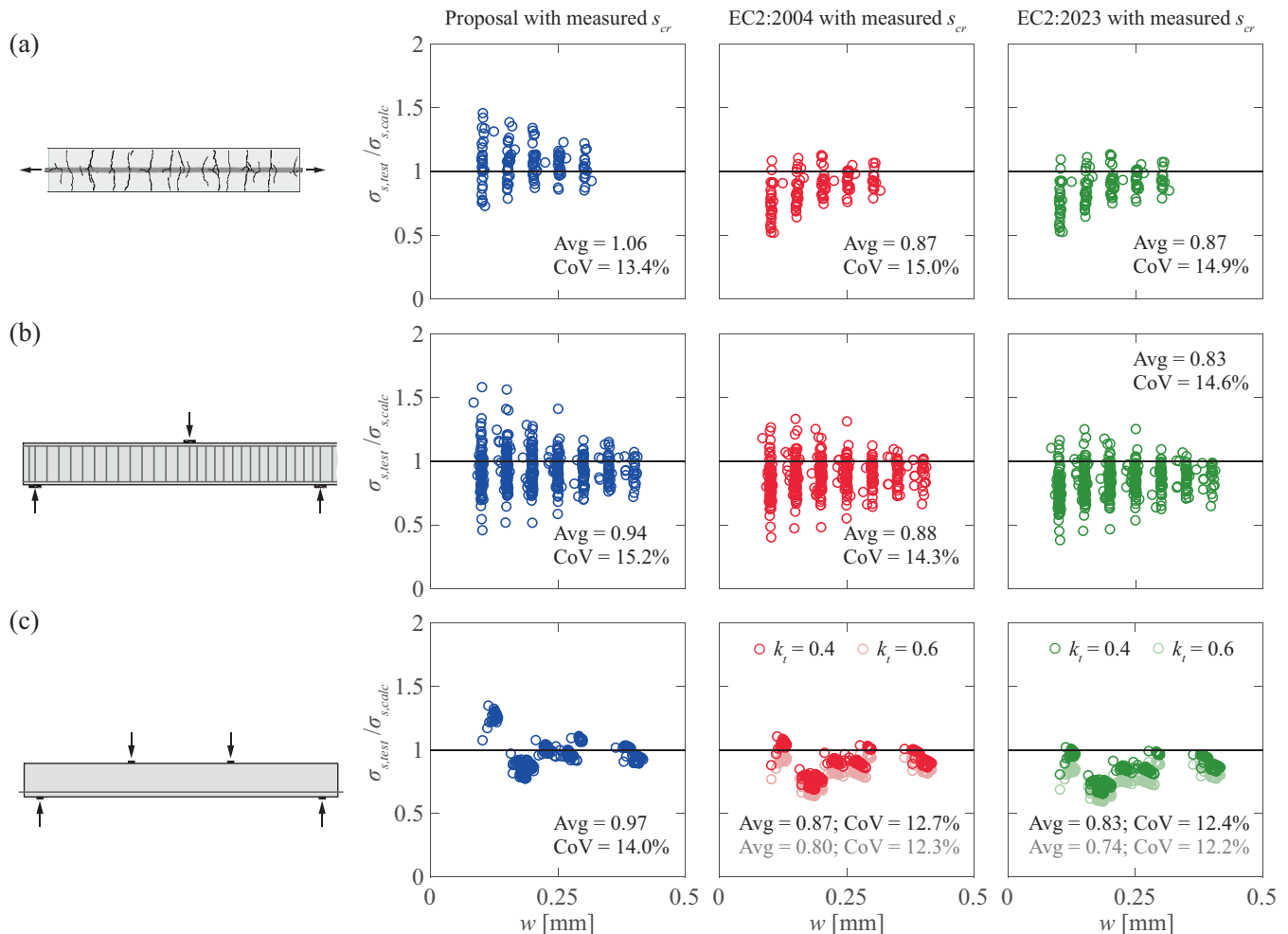

FIGURE 14 Ratio of experimental over calculated steel stress as a function of the crack width: (a) tension specimen TC11; (b) all beam specimens of series SM10; and (c) for the maximum cyclic force for specimens SC76 and SC77.

widths, both models underestimate the steel strain reduction, which leads to the overestimation of the stress. The reduction of the dispersion for larger crack widths can be explained by the fact that the bond stress has a constant influence on the crack width in terms of absolute values (see Figure 2b). Therefore, it has a smaller relative impact for large crack widths, which leads to lower relative errors for larger stresses. The small differences between the results using EC2:2004 and EC2:2023 are due to the differences in the definition of the effective reinforcement ratio.

Figure 14c shows the results for the cyclic tests at the maximum force of each cycle. The proposed bond values lead to a certain improvement in the estimation. It must be noted that during the unloading phase bond stresses decrease and can reach negative values.[33,35,87] Negative tension stiffening and the imperfect closure of cracks lead to stresses in the reinforcement that can be larger than the prediction according to simplified cross section analysis.[33,35,88,89] This part of the response is out of the scope of this paper. Nevertheless, this plays a significant role in the stress variation in the reinforcement and must be considered for the fatigue assessment.

The crack width considered in this analysis was measured on the surface of the specimens. For the considered range of covers, the results indicate that the response is well captured by the model based on the measured crack spacing. For larger covers, further validations are required. It must be noted that, as the crack width typically increases with the cover,[56,58,64,65] the application of the model will likely lead to an overestimation of the stress in the bar for large covers.

The assumption of a constant bond stress used in current code formulations is reasonable and practical given the inherent uncertainty and variability of the cracking phenomenon. However, the lower experimental bond stresses could have an influence in the crack spacing estimation. This is visible in the results from series SM10 where the calculated maximum crack spacing is actually close to the average of the experimental results (see Figure 8d). Further research is required to confirm this potential effect.

7 | CONCLUSIONS

This paper presents the results of an experimental program and an analytical investigation to improve the current understanding of cracking in structural elements, with the aim of estimating the stress in the reinforcement based on crack width measurements. The main findings of this research are:

1. The measured average bond stresses are in most cases lower than the values proposed by current standards, with the exception of the stirrups in the beam tests that showed in some cases larger values. This could have a relevant influence in the estimation of the crack spacing.

2. The decrease of bond stresses for cyclic loading concentrates in the first 10 to 15 cycles. After that, the decrease progresses at a slower pace. This seems to depend on the stress variation range. Further research is required to confirm these findings.

3. In cases where the flexural cracks develop at the transverse reinforcement location, the presence of transverse reinforcement does not guarantee its activation as confinement for bond stress development between cracks along the longitudinal reinforcement.

4. An expression to estimate the average bond stresses considering the crack width, the casting conditions, the type of loading (monotonic or cyclic) and the presence of longitudinal cracks along the bar is proposed. The expression is derived from the integration of the local bond–slip relationship, accounting for the presence of secondary cracks. The estimated values show good agreement with the experimental values for short-term monotonic loading.

5. The slip-based model gives good results for the bar stress–crack width response, provided that the average bond stresses are adjusted. Using this model, a reasonable estimation of the bar stress as a function of the measured crack width can be obtained for the investigated tests. Further research is required with larger clear covers.

6. The estimated bar stresses using the slip-based model and the proposed expression for the average bond stresses perform better than current code formulations. The code formulations tend to overestimate the bar stress due to the inherent assumptions for the calculation of the relative mean strain.

7. Shrinkage induced strains have a significant influence on cracking and the estimated bar stresses. However, neglecting its influence leads to an overestimation of the bar stress.

NOTATION
Lower case Latin characters

b_R	rib width
b_w	beam width
c	clear concrete cover
d	beam effective depth
f_c	concrete compressive strength
f_{cm}	mean concrete cylinder compressive strength

f_{ct} concrete tensile strength

f_{ctm} mean concrete tensile strength

f_R bond index of the reinforcement

f_{ym} mean yield strength of the longitudinal reinforcement

f_{ywm} mean yield strength of the shear reinforcement

h beam height

h_c depth of the compression zone in a section subjected to bending

k_{cyc} average bond stress reduction factor due to cyclic loading

k_{lc} average bond stress reduction factor due to longitudinal cracks along the bar

k_{sr} average bond stress adjustment factor

l_{cr} transfer length

n ratio of the steel elastic modulus divided by the concrete elastic modulus

s stirrup spacing

s_{cr} crack spacing

s_R rib spacing

$s_{R,clear}$ clear rib spacing at the top of the lugs

v beam test mid-span deflection

w crack width component in the direction of the reinforcement

w_{lc} crack width of the longitudinal crack along the reinforcements

x coordinate along x axis

Upper case Latin characters

A transverse cross section

A_c concrete area in the transverse cross section

E_c elastic modulus of the concrete

E_s elastic modulus of the reinforcement

F tensile force applied to the concrete ties

N number of cycles

V shear force

$V_{cyc,max}$ maximum shear force during cyclic loading

$V_{cyc,min}$ minimum shear force during cyclic loading

V_{max} maximum measured shear force

Lower case Greek characters

δ_{sc} relative slip between the bar and the concrete

ε_c concrete strain

ε_{cs} unrestrained shrinkage strain

ε_s steel strain

η_2 factor for to account for casting position

λ bond reduction factor near the crack

ρ_f flexural reinforcement ratio as/(d·bw)

ρ_t tensile reinforcement ratio as/a

ρ_w shear reinforcement ratio asw/(s·bw)

$\sigma_{cyc,max}$ maximum nominal stress in the reinforcement for the maximum force during cyclic loading

$\sigma_{cyc,min}$ minimum nominal stress in the reinforcement for the maximum force during cyclic loading

τ_b local bond stress

$\tau_{b,avg}$ average bond stress over a certain length

$\tau_{bu,po}$ maximum bond stress for pull-out failure

$\tau_{bu,sc}$ maximum bond stress for splitting with confinement

$\tau_{bu,su}$ maximum bond stress for splitting in unconfined conditions

χ_s reinforcement bar curvature

Other characters

Ø   bar nominal diameter

DATA AVAILABILITY STATEMENT

The data that support the findings of this study are available from the corresponding author upon reasonable request.

REFERENCES

1. Eurocode. Eurocode 2: design of concrete structures—Part 1–1: general rules and rules for buildings. Brussels: European Committee for Standardization (CEN); 2004.

2. fib. fib model code for concrete structures 2010. 1st ed. UK: fib; 2013.

3. OFROU. Directive ASTRA 62016: Guide pour les inspecteurs d'ouvrages d'art [Édition 2021 V1.20]. Switzerland: Office fédéral des routes; 2021. p. 85.

4. Zaborac J, Athanasiou A, Salamone S, Bayrak O, Hrynyk TD. Evaluation of structural cracking in concrete [Final Report (FHWA/TX-19/0-6919-1)]. Austin, USA: Center for Transportation Research at The University of Texas at Austin; 2019. p. 172.

5. Monney F, Fernández RM, Muttoni A. Influence of amount of shear reinforcement and its post-yield response on the shear resistance of reinforced concrete members. Struct Concr. 2022; 24(1):1–33.

6. Bell B. European railway bridge demography D1.2. Sustainable bridges—assessment for future traffic demands and longer lives; 2004. p. 15.

7. Naraniecki H, Marx S. Zustandsentwicklung und -prognose von Eisenbahnbrücken, 60. Hannover, Germany: Forschungskolloquium des Deutschen Ausschusses für Stahlbeton; 2019. p. 103–18.

8. OFROU. Rapport d'état des routes nationales [Etat au 31.12.2022, Edition 2023]. Switzerland: Office fédéral des routes; 2023. p. 56.

9. Croce P. Impact of road traffic tendency in Europe on fatigue assessment of bridges. Appl Sci. 2020;10:30.

10. Capros P, De Vita A, Tasios N, Papadopoulos D. EU energy, transport and GHG emissions trends to 2050. Luxembourg:

European Commission, Directorate-General for Energy, Directorate-General for Climate Action and Directorate-General for Mobility and Transport; 2013. p. 173. https://doi.org/10.2833/17897

11. Treacy MA, Brühwiler E. A direct monitoring approach for the fatigue safety verification of construction joint details in an existing post-tensioned concrete box-girder bridge. Eng Struct. 2015;88:189–202.

12. Saliger R. Hochwertige Stähle im Eisenbetonbau (High-Grade Steel in Reinforced Concrete). Proceedings of the 2nd congress of the international association for bridge and structural engineering (IABSE). Volume 2. IABSE: Berlin-Munich, Germany; 1936. p. 303–23.

13. Thomas FG. Cracking in reinforced concrete. Struct Eng. 1936;14(7):298–320.

14. Broms BB. Crack width and crack spacing in reinforced concrete members. ACI J Proc. 1965;62(10):1237–56.

15. CEB. Fissuration, Comité Euro-International du béton. Bulletin d'Information. 1967;61:253.

16. Ferry-Borges J. Cracking and deformability of reinforced concrete beams. Vol 26. Zurich, Switzerland: International Association of Bridge and Structural Engineering; 1966. p. 75–95.

17. Borosnyói A, Balázs GL. Models for flexural cracking in concrete: the state of the art. Struct Concr. 2005;6(2):53–62.

18. Lapi M, Orlando M, Spinelli P. A review of literature and code formulations for cracking in R/C members. Struct Concr. 2018;19(5):1255–535.

19. Van Der Esch A, Wolfs R, Fennis S, Roosen M, Wijte S. Categorization of formulas for calculation of crack width and spacing in reinforced concrete elements. Struct Concr. 2023;25(1):17.

20. Balázs GL. Cracking analysis based on slip and bond stresses. ACI Mater J. 1993;90(1):340–8.

21. CEB. CEB-FIP Model Code 1990. London, UK: Comité Euro-International du Béton (CEB); 1993. p. 460.

22. Noakowski P. Nachweisverfahren für Verankerung, Verformung, Zwangsbeanspruchung und Rissbreite. Vol 394. Germany: Deutscher Ausschuss für Stahlbeton; 1988. p. 75.

23. Sigrist V. Zum Verformungsvermögen von Stahlbetonträgern [Dissertation, No. 11169]. Zürich, Switzerland: ETHZ; 1995. p. 159.

24. Bado MF, Casas J-R, Kaklauskas G. Distributed sensing (DOFS) in reinforced concrete members for reinforcement strain monitoring, crack detection and bond–slip calculation. Eng Struct. 2021;226:111385.

25. Corres E, Muttoni A. Bond of steel reinforcement based on detailed measurements: results and interpretations. Struct Concr. 2023;24(6):7173–204.

26. Metelli G, Plizzari G. Influence of the relative rib area on bond behaviour. Mag Concr Res. 2014;66(6):277–94.

27. Campana S, Fernández RM, Anastasi A, Muttoni A. Analysis of shear-transfer actions on one-way RC members based on measured cracking pattern and failure kinematics. Mag Concr Res. 2013;56(6):386–404.

28. Calvi PM. A theory for the shear behaviour of cracks providing a basis for the assessment of cracked reinforced concrete structures [PhD thesis]. Canada: University of Toronto; 2015. p. 367.

29. Shima H, Chou LL, Okamura H. Bond characteristics in post-yield range of deformed bars. Proc JSCE Transl. 1987;378/v-6:113–24.

30. Maekawa K, Pimanmas A, Okamura H. Nonlinear mechanics of reinforced concrete. London: Spon Press; 2003. p. 768.

31. Brault A, Hoult NA, Lees JM. Development of a relationship between external measurements and reinforcement stress. Proc SPIE. 2015;9435:12.

32. Carmo RNF, Valença J, Silva D, Dias da Costa D. Assessing steel strains on reinforced concrete members from surface cracking patterns. Construct Build Mater. 2015;98:265–75.

33. Cantone R, Fernández RM, Muttoni A. A detailed view on the rebar-to-concrete interaction based on refined measurement techniques. Eng Struct. 2020;226:19.

34. Galkovski T, Mata FJ, Kaufmann W. Experimental investigation of bond and crack behaviour of reinforced concrete ties using distributed fibre optical sensing and digital image correlation. Eng Struct. 2023;292:24.

35. Lemcherreq Y, Zanuy C, Vogel T, Kaufmann W. Experimental and analytical assessment of fatigue damage in reinforced concrete tension members. Eng Struct. 2023;289:23.

36. Galkovski T, Mata FJ, Kaufmann W. Effective reinforcement ratio of RC beams: validation of modelling assumptions with high-resolution strain data. Struct Concr. 2022;23(3):1353–69.

37. Poldon JJ, Hoult NA, Bentz EC. Distributed sensing in large reinforced concrete shear test. ACI Struct J. 2019;116(5):235–45.

38. Bado MF, Casas J-R, Dey A, Berrocal C, Kaklauskas G, Fernandez I, et al. Characterization of concrete shrinkage induced strains in internally-restrained RC structures by distributed optical fiber sensing. Cem Concr Compos. 2021;120:12.

39. Davis MB, Hoult NA, Bajaj S, Bentz EC. Distributed sensing for shrinkage and tension stiffening measurement. ACI Struct J. 2017;114:755–66.

40. Corres E, Muttoni A. Local bond-slip model based on mechanical considerations. Eng Struct. 2024;314(1):118190.

41. Hordijk DA. Local approach to fatigue of concrete. Delft, Netherlands: Technische Universiteit Delft, [Thesis]; 1991.

42. Bischoff PH. Effects of shrinkage on tension stiffening and cracking in reinforced concrete. Can J Civ Eng. 2001;21(3):363–74.

43. Gribniak V, Kaklauskas G, Bacinskas D. State-of-art review of shrinkage effect on cracking and deformations of concrete bridge elements. Baltic J Road Bridge Eng. 2007;2(4):183–93.

44. García R, Pérez CA. Influence of casting position on cracking behavior of reinforced concrete elements and evaluation of latest proposal for EN-1992 and MC2020: experimental study. Struct Concr. 2022;23(5):2910–27.

45. Pérez CA, García R, Gribniak V, Rimkus A. Tension versus flexure: reasons to modify the formulation of MC 2010 for cracking. Struct Concr. 2020;21(5):2101–23.

46. fib. fib model code for concrete structures 2020. fib; 2024. p. 748. https://fib-international.org/

47. Eurocode. Eurocode 2: design of concrete structures—Part 1-1: general rules and rules for buildings, bridges and civil engineering structures, EN 1992-1-1. Brussels, Belgium: European Committee for Standardization (CEN); 2023. p. 405.

48. Marti P, Alvarez M, Kaufmann W, Sigrist V. Tension chord model for structural concrete. Struct Eng Int IABSE. 1998;8(4):287–98.

49. fib. Constitutive modelling of high strength/high performance concrete. Vol 42. Lausanne, Switzerland: Fédération Internationale du Béton, *fib* Bulletin; 2008. p. 134.

50. Cavagnis F, Fernández RM, Muttoni A. Shear failures in reinforced concrete members without transverse reinforcement: an

analysis of the critical shear crack development on the basis of test results. Eng Struct. 2015;103:157–73.

51. Kaklauskas G, Sokolov A, Sakalauskas K. Strain compliance crack model for RC beams: primary versus secondary cracks. Eng Struct. 2023;281:13.

52. Leonhardt F. Cracks and crack control in concrete structures. PCI J. 1988;33(4):124–45. https://doi.org/10.15554/pcij.07011988.124.145

53. Rasmussen AB. Modelling of reinforced concrete in the serviceability limit state [PhD thesis]. Denmark: Aarhus University Department of Engineering; 2019. p. 213.

54. Burns C. Serviceability analysis of reinforced concrete based on the tension chord model [PhD thesis]. Zurich: ETHZ; 2011. p. 160.

55. Goto Y. Cracks formed in concrete around deformed tension bars. ACI J. 1971;68(4):244–51.

56. Gribniak V, Rimkus A, Pérez CA, Sokolov A. Cracking of concrete prisms reinforced with multiple bars in tension—the cover effect. Eng Struct. 2020;220:19.

57. Windisch A. Crack control: An advanced calculation model. Part I: Review of classic tests, Concrete Structures. Annu Tech J Hung Group fib. 2016;17:41–7.

58. Yannopoulos PJ. Variation of the concrete crack widths through cover to reinforcement. Mag Concr Res. 1989;41(147):63–8.

59. fib. Bond of reinforcement in concrete [Fédération Internationale du Béton—*fib* Bulletin n°10; State-of-art report prepared by Task Group Bond models]. Vol 10. Lausanne, Switzerland: *fib* Bulletin; 2000. p. 427.

60. Pérez CA, Corres PH, Peset IJ, Giraldo SA. Cracking of RC members revisited: influence of cover, ϕ/ρs, ef and stirrup spacing—an experimental and theoretical study. Struct Concr. 2013;14(1):69–78.

61. Eligehausen R, Popov P, Bertero V. Local bond stress–slip relationships of deformed bars under generalized excitations [UCB/EERC, 83/23]. 1983.

62. Kreller H. Zum nichtlinearen Trag- und Verformungsverhalten von Stahlbetonstabtragwerken unter Last- und Zwangeinwirkung. Germany: Institut für Werkstoffe im Bauwesen, Mitteilungen, Universität Stuttgart; 1989. p. 214.

63. Fernández RM, Muttoni A, Gambarova P. Analytical modelling of the pre- and post-yield behaviour of bond in reinforced concrete. ASCE J Struct Eng. 2007;133(10):1364–72.

64. Borosnyói A, Snóbli I. Crack width variation within the concrete cover of reinforced concrete members. Epitoanyag. 2010;62(3):70–4.

65. Husain SI, Ferguson PM. Flexural crack widths at the bars in reinforced concrete beams. Austin, USA: Centrale nationale d'alarme, the University of Texas at Austin; 1968. p. 41.

66. ISO EN ISO 15630-1. Steel for the reinforcement and prestressing of concrete—test methods—Part 1: reinforcing bars, wire rod and wire. Belgium: European Committee For Standardization CEN; 2019. p. 36.

67. Correlated Solutions. Vic-3D 8 software manual, Version 8.4. 2021.

68. Luna Technologies Inc. ODiSI 6000 Series User Guide, 99. 2020.

69. Gehri N, Mata FJ, Kaufmann W. Refined extraction of crack characteristics in large-scale concrete experiments based on digital image correlation. Eng Struct. 2022;251-A:21.

70. Galkovski T, Lemcherreq Y, Mata FJ, Kaufmann W. Fundamental studies on the use of distributed fibre optical sensing on concrete and reinforcing bars. Sensors. 2021;21(22):24.

71. Lemcherreq Y, Galkovski T, Mata FJ, Kaufmann W. Application of distributed fibre optical sensing in reinforced concrete elements subjected to monotonic and cyclic loading. Sensors. 2022;22(5):28.

72. Clark AP. Bond of concrete reinforcing bars. J Res Natl Bur Stand. 1949;43:565–79.

73. Moccia F, Fernández RM, Metelli G, Muttoni A, Plizzari G. Casting position effects on bond performance of reinforcement bars. Struct Concr. 2021;22(3):21.

74. Tammo K. Crack behavior near reinforcing bars in concrete structures. ACI Struct J. 2009;106(3):259–67.

75. Cavagnis F, Fernández RM, Muttoni A. A mechanical model for failures in shear of members without transverse reinforcement based on development of a critical shear crack. Eng Struct. 2018;157:300–15.

76. Fernández RM, Muttoni A, Sagaseta J. Shear strength of concrete members without transverse reinforcement: a mechanical approach to consistently account for size and strain effects. Eng Struct. 2015;99:360–72.

77. Tilly GP. Fatigue of steel reinforcement bars in concrete: a review. Fatigue Eng Mater Struct. 1979;2:251–68.

78. Zheng H, Abel AA. Fatigue properties of reinforcing steel produced by TEMPCORE process. J Mater Civ Eng. 1999;11(2):158–65.

79. Rehm G. Kriterien zur Beurteilung von Bewehrungsstäben mit hochwertigen Verbund. Berlin, Germany: Stahlbetonbau, Berichte aus Forschung und Praxis, Verlag Wilhelm Ernst & Sohn; 1969. p. 79–96.

80. Brantschen F, Faria DMV, Fernández RM, Muttoni A. Bond behaviour of straight, hooked, U-shaped and headed bars in cracked concrete. Struct Concr. 2016;17(5):799–810.

81. Cedolin L, Dei PS, Iori I. Analisi sperimentale del processo di formazione della frattura nel calcestruzzo. Vol 3. Milan, Italy: Studi E Ricerche, Politecnico di Milano; 1981. p. 47–74.

82. Cedolin L, Dei PS, Iori I. Comportamento a trazione del calcestruzzo. Vol 5. Milan, Italy: Studi E Ricerche, Politecnico di Milano; 1983. p. 23–46.

83. CEB. Structures en béton sous actions sismiques [State of the Art Report, Bulletin 131]. Rome, Italy: CEB (Comité euro-international du béton); 1979.

84. Balázs GL. Fatigue of bond. ACI Mater J. 1991;99-M64:620–9.

85. Debernardi PG, Taliano M. An improvement to Eurocode 2 and *fib* model code 2010 methods for calculating crack width in RC structures. Struct Concr. 2016;17(3):365–76.

86. Lemcherreq Y, Haefliger S, Kaufmann W. Discontinuous yielding in bare and embedded reinforcing bars: implications on the determination of steel and bond shear stresses from strain measurements. Eng Struct. 2023;278:20.

87. Giuriani E. Experimental investigation on bond–slip law of deformed bars in concrete. Delft, Netherlands: IABSE Colloquium; 1981. p. 121–42.

88. Muttoni A, Fernández RM. Concrete cracking in tension members and application to deck slabs of bridges. ASCE J Bridge Eng. 2007;12:646–53.

89. Zanuy C, De La Fuente P, Albajar L. Estimation of parameters defining negative tension stiffening. Eng Struct. 2010;32(10): 3355–62.

90. fib. Bond and anchorage of embedded reinforcement: background to the fib model code for concrete structures 2010. Vol 72. Lausanne, Switzerland: Fédération Internationale du Béton, *fib* Bulletin; 2014. p. 161.

AUTHOR BIOGRAPHIES

Enrique Corres, School of Architecture, Civil and Environmental Engineering, Ecole Polytechnique Fédérale de Lausanne, Lausanne, Switzerland. Email: enrique.corressojo@epfl.ch.

Aurelio Muttoni, School of Architecture, Civil and Environmental Engineering, Ecole Polytechnique Fédérale de Lausanne, Lausanne, Switzerland. Email: aurelio.muttoni@epfl.ch.

APPENDIX A

ANALYTICAL EXPRESSION DEVELOPMENT

Based on the equilibrium and compatibility conditions of the differential element shown in Figure 1b and assuming a linear elastic behavior of both steel and concrete and no external forces acting on the element, the differential equation governing the tie segment response is given by Equation (A.1).

$$\frac{d^2\delta_{sc}}{dx^2} = \frac{4\tau_b(x)}{\varnothing E_s} + \frac{\pi\varnothing\tau_b(x)}{A_c E_c}. \tag{A.1}$$

Assuming that the first crack appears when the concrete stress reaches f_{ct}, due to compatibility of deformations the cracking axial force is determined by Equation (A.2). The stress in the reinforcement before and after cracking can be calculated using Equations (A.3) and (A.4) at the cracked section:

$$N_{cr} = \frac{f_{ct}}{E_c}(A_c E_c + A_s E_s), \tag{A.2}$$

$$\sigma_{sB} = \frac{f_{ct}}{E_c}E_s = \varepsilon_{cr}E_s, \tag{A.3}$$

$$\sigma_{sC} = \frac{f_{ct}}{\rho}[1 + (n-1)\rho]. \tag{A.4}$$

Given the stress variation, the required transfer length l_{cr} as a function of the average bond stress $\tau_{b,avg}$ can be determined using Equation (A.5):

$$l_{cr} = \frac{\varnothing}{4\tau_{b,avg}}\Delta\sigma_s = \frac{\varnothing f_{ct}}{4\tau_{b,avg}}\frac{1-\rho}{\rho}. \tag{A.5}$$

The crack width in the crack formation stage is therefore:

$$w = \frac{l_{cr}\sigma_{sC}}{E_s} = \frac{\varnothing f_{ct}^2}{4\tau_b E_s}\frac{(1-\rho)(1+(n-1)\rho)}{\rho^2}. \tag{A.6}$$

This expression can be generalized for any stress σ_{sC}, as shown in Equation (A.6):

$$w = \frac{\varnothing\sigma_{sC}^2}{4\tau_b E_s}\frac{1-\rho}{1+(n-1)\rho}. \tag{A.6}$$

In the stabilized cracking stage, the distance between cracks is smaller than the transfer length. Therefore, the tensile strength of the concrete cannot be reached between cracks and no further principal crack develops (secondary cracks may develop). In these conditions, the crack width for a given stress can be calculated considering that the maximum axial force that can be taken by the concrete as a function of the crack spacing and the average bond stress. The resulting equation is:

$$w = \frac{s_{cr}}{E_s}\left[\sigma_{sC} - \frac{s_{cr}\tau_{b,avg}}{\varnothing}\frac{1+(n-1)\rho}{1-\rho}\right]. \tag{A.7}$$

Due to the reinforcement, the shrinkage strains ($\varepsilon_{cs} < 0$) are partially restrained, which causes tensile forces in the concrete and compression in the reinforcement. From compatibility and equilibrium conditions, the initial strain can be determined using Equation (A.8):

$$\varepsilon_{ci} = \varepsilon_{si} = \frac{1-\rho}{1+(n-1)\rho}\varepsilon_{cs}. \tag{A.8}$$

As a consequence of this initial stress-state, the cracking force is reduced:

$$N_{cr,cs} = N_{cr}\left[1 + \frac{n\rho}{1+(n-1)\rho}\frac{\varepsilon_{cs}}{f_{ct}/E_c}\right]. \tag{A.9}$$

Nevertheless, both the cumulative difference of strains remains the same because both strain diagrams are shifted by the unrestrained shrinkage strain (see Figure 1c,d). Consequently, assuming the same bond distribution, the anchorage length and the crack width are the same for a lower stress in the reinforcement. For the stabilized cracking phase, the effect of shrinkage affects the average concrete strains as shown in Equation (A.10):

$$w = \frac{s_{cr}}{E_s}\left[\sigma_{sC} - \frac{s_{cr}\tau_{b,avg}}{\varnothing}\frac{1+(n-1)\rho}{1-\rho} - E_s\varepsilon_{cs}\right]. \tag{A.10}$$

APPENDIX B

CONSIDERED LOCAL BOND–SLIP RELATIONSHIPS

The bond–slip relationships for monotonic loading were investigated by the authors in a separate publication.[40] The general expression of the segments composing the curve is defined in Equation (B.1) (see Figure 11a):

$$\begin{aligned}
\tau_b &= \tau_{b,max}(\delta_{sc}/\delta_{sc1})^\alpha && \text{for } 0 \le \delta_{sc} \le \delta_{sc1}, \\
\tau_b &= \tau_{b,max} && \text{for } \delta_{sc1} < \delta_{sc} \le \delta_{sc2}, \\
\tau_b &= \tau_{b,max} - (\tau_{b,max} - \tau_{bf})(\delta_{sc} - \delta_{sc2})/(\delta_{sc3} - \delta_{sc2}) && \text{for } \delta_{sc2} \\
&\quad < \delta_{sc} \le \delta_{sc3}, \\
\tau_b &= \tau_{bf}(1 - (\delta_{sc} - \delta_{sc3})/(\delta_{sc4} - \delta_{sc3})) && \text{for } \delta_{sc3} < \delta_{sc} \le \delta_{sc4}.
\end{aligned}$$
$$\tag{B.1}$$

TABLE B1   Bond–slip relationship parameters.[40]

Param.	Well-confined	Moderate confinement	Unconfined
τ_{bu}	$\tau_{bu,po} = 0.5 f_{cm}\left(\frac{30}{f_{cm}}\right)^{1/6}\left(\frac{20}{\varnothing}\right)^{1/8}$	$\tau_{bu,sc} = \tau_{bu,su} + \left(\tau_{bu,po} - \tau_{bu,su}\right)k_{conf}$	$\tau_{bu,su} = 7.1\left(\frac{f_{cm}}{30}\right)^{0.25}\left(\frac{20}{\varnothing}\right)^{0.2}$
τ_{bf}	$0.4 \cdot \tau_{bu}$	$\tau_{bf,sc} = \tau_{bf,su} + \left(\tau_{bf,po} - \tau_{bf,su}\right)k_{conf}$	0
δ_{sc1}	$1.0 \cdot \frac{\varnothing}{20}\cdot\left(\frac{30}{f_{cm}}\right)^{1/3}\left(\frac{0.08}{f_R}\right)^{1/5}$	$\delta_{sc1,sp} = \delta_{sc1,po}\left(\frac{\tau_{bu,sp}}{\tau_{bu,po}}\right)^{1/\alpha}$	$\delta_{sc1,su} = \delta_{sc1,po}\left(\frac{\tau_{bu,su}}{\tau_{bu,po}}\right)^{1/\alpha}$
δ_{sc2}	$2 \cdot \delta_{sc1}$	$\delta_{sc2,sc} = \delta_{sc2,su} + \left(\delta_{sc2,po} - \delta_{sc2,su}\right)k_{conf}$	δ_{sc1}
δ_{sc3}	$s_{R,clear}$	$\delta_{sc3,sc} = \delta_{sc3,su} + \left(\delta_{sc3,po} - \delta_{sc3,su}\right)k_{conf}$	$1.2 \cdot \delta_{sc1}$
δ_{sc4}	$3 \cdot s_R$	$\delta_{sc4,sc} = \delta_{sc4,su} + \left(\delta_{sc4,po} - \delta_{sc4,su}\right)k_{conf}$	$1.2 \cdot \delta_{sc1}$
α	0.4		

The factor to account for the cover and transverse reinforcement proposed in MC2010 is used for the definition of the confinement conditions.[2,90] This factor is limited to a value of 1.5, that corresponds to the confinement when $c = 5\varnothing$. A minimum value of 1 is set, that corresponds to the confinement when $c = 1\varnothing$. The normalized factor can be determined using Equation (B.2):

$$k_{conf} = \frac{1}{0.5}\left[\left(\frac{c_{min}}{\varnothing}\right)^{0.25}\left(\frac{c_{max}}{c_{min}}\right)^{0.1} - 1\right] \quad k_{conf} \in [0,1],$$
$$c_{min} = \min\left(c_s/2, c_x, c_y\right),$$
$$c_{max} = \min\left(c_s/2, c_x, c_y\right),$$

(B.2)

where c_{min} and c_{max} are minimum and maximum covers (or half bar spacing c_s).[2] The stirrup contribution is not considered as discussed in Sections 4.2 and 5.

Three confinement conditions are defined accordingly:

- Well-confined: $k_{conf} = 1$, corresponding to covers $\geq 5\varnothing$.
- Unconfined: $k_{conf} = 0$, corresponding to covers $= 1\varnothing$.
- Moderate confinement: $0 < k_{conf} < 1$, intermediate situations.

The main parameters of the proposed bond–slip relationship for the three types of confinement are summarized in Table B1.